Geophys. J. Int. Revised

Ground Motion Response to a M_L 4.3 Earthquake Using Co-Located Distributed Acoustic Sensing and Seismometer Arrays

Herbert F. Wang[1*], Xiangfang Zeng[1,2], Douglas E. Miller[3], Dante Fratta[4], Kurt L. Feigl[1], Clifford H. Thurber[1], and Robert J. Mellors[5]

1. Department of Geoscience, University of Wisconsin–Madison, Madison, WI 53706, USA
2. State Key Laboratory of Geodesy and Earth's Dynamics, Institute of Geodesy and Geophysics, Chinese Academy of Sciences, Wuhan, 430077, China
3. Silixa, Ltd, 230 Centennial Park, Centennial Avenue, Elstree, Hertfordshire WD6 3SN, UK and Earth Resource Laboratory, Massachusetts Institute of Technology, Cambridge, MA 02139-4307, USA
4. Geological Engineering, Department of Civil and Environmental Engineering, University of Wisconsin–Madison, Madison, WI 53706, USA
5. Atmospheric, Earth, and Energy Division, Lawrence Livermore National Laboratory, Livermore, CA 94550

* Corresponding Author. Email address: hfwang@wisc.edu.

March 19, 2018

Summary

The PoroTomo research team deployed two arrays of seismic sensors in a natural laboratory at Brady Hot Springs, Nevada in March 2016. The 1500 m (length) by 500 m (width) by 400 m (depth) volume of the laboratory overlies a geothermal reservoir. The surface Distributed Acoustic Sensing (DAS) array consisted of 8700 m of fiber-optic cable in a shallow trench, including 340 m in a well. The conventional seismometer array consisted of 238 three-component geophones. The DAS cable was laid out in three parallel zig-zag lines with line segments approximately 100 meters in length and geophones were spaced at approximately 60-meter intervals. Both DAS and conventional geophones recorded continuously over 15 days during which a moderate-sized earthquake with a local magnitude of 4.3 was recorded on March 21, 2016. Its epicenter was approximately 150-km south-southeast of the laboratory. Several DAS line segments with co-located geophone stations were used to compare signal-to-noise (SNR) ratios in both time and frequency domains and to test relationships between DAS and geophone data. The ratios were typically within a factor of five of each other with DAS SNR often greater for P-wave but smaller for S-wave relative to geophone SNR. The SNRs measured for an earthquake can be better than for active sources, because the earthquake signal contains more low frequency energy and the noise level is also lower at those lower frequencies.

Amplitudes of the sum of several DAS strain-rate waveforms matched the finite difference of two geophone waveforms reasonably well, as did the amplitudes of DAS strain waveforms with particle-velocity waveforms recorded by geophones. Similar agreement was found between DAS and geophone observations and synthetic strain seismograms. The combination of good SNR in the seismic frequency band, high-spatial density, large N, and highly accurate time control among individual sensors suggests that DAS arrays have potential to assume a role in earthquake seismology.

Keywords: Distributed Acoustic Sensing (DAS), ground motion, strain, particle velocity, signal-to-noise ratio, earthquake seismology

Introduction

Distributed Acoustic Sensing (DAS) for sensing ground motion has been applied to geophysical studies (Parker et al., 2014; Bakku, 2015). DAS technology has the potential to image the subsurface using dense arrays whose spatial resolution is on the order of ten meters and whose dimensions can be tens of kilometers given the relatively low cost of fiber-optic cable and currently available interrogator and processing technology. The flexibility of fiber-optic cable allows for many possible geometric configurations. Its use for Vertical Seismic Profiling (VSP) in oil-and-gas reservoirs and CO_2 sequestration sites has been demonstrated in several case studies (Johannessen et al. 2012; Miller et al, 2012; Madsen et al. 2013; Mateeva et al. 2014; Miller et al, 2016). The fiber-optic cable can be permanently cemented behind casing in a borehole to be used for repeat surveys. Fewer examples exist of horizontal deployments. The University of Wisconsin-Madison and Silixa, Ltd. have conducted four trials beginning with a 90-meter layout on lake ice (Castongia et al., 2017), a 762-meter layout at Garner Valley, California (Zeng et al., 2017a; Lancelle et al., 2017), a 9-km array at the Brady Hot Springs, NV geothermal site (Feigl and PoroTomo Team, 2017; Zeng et al., 2017b), and a 250-m array in an operating, underground limestone mine in N. Aurora, Illinois (Wang et al., 2017). Likewise, Lawrence Berkeley National Laboratory (LBNL) and Silixa have an extensive program of deploying fiber-optic cable layouts of increasing spatial size for monitoring carbon sequestration and permafrost sites using a 150-meter receiver line and a 36-kilometer array at the Otway (Australia) carbon sequestration site (Daley et al. 2013; Freifeld et al., 2016; Yavuz et al., 2016; Dou et al., 2017; Lindsey et al., 2017). A 17-kilometer DAS array at the Nevada Test Site has been reported by Mellors et al. (2014).

This paper utilizes data from the Brady Hot Springs 9-km DAS array together with a co-located array of 238 three-component geophones (Fig. 1) to assess and correlate the different physical measurements obtained with the two sets of arrays. Understanding the relationship between DAS and geophone recordings is foundational for plans to apply DAS in earthquake seismology. During the 15 days of continuous recording in March 2016, both arrays recorded data from a M_L 4.3 earthquake, whose epicenter at Hawthorne, NV, was about 150-km south-southeast of the field site (Fig. 2). The focal depth was 9.9 km. The data from this earthquake are the basis for examining how DAS records ground motion as a sensor for use in earthquake seismology.

The paper is organized as follows. 1) First, a brief overview of the Brady field experiment is provided. 2) Second, the principles of DAS are described. 3) Finally, the different characteristics of DAS are illustrated and compared with geophone responses for the M_L 4.3 Hawthorne earthquake.

Brady Hot Springs

The DAS array at Brady Hot Springs was deployed as part of a large, coordinated hydrogeophysical experiment for Poroelastic Tomography (PoroTomo) conducted over a two-week period in March 2016 in a geothermal field operated by Ormat Technologies (Feigl and PoroTomo Team, 2017). The field laboratory encompasses a volume that covered a surface area of 1500 m by 500 m down to a depth of 400 m (Fig. 1). The subsurface geology consists of several hundred meters of alluvium beneath which is the geothermal reservoir of layered Tertiary volcanic rocks that overlie Mesozoic crystalline intrusions (e.g., Siler & Faulds, 2013; Jolie et al., 2015). Subsidence has been measured using geodetic techniques and modeled using elastic dislocations (Ali et al., 2016).

A variety of sensors were emplaced throughout the volume. The 8700-meter DAS fiber-optic sensing array was installed horizontally in three, parallel zig-zag patterns in a trench approximately 0.50 m in depth (Fig. 1). The array included approximately 360 meters of cable emplaced in a borehole in the southwest corner of the layout. Results for the borehole DAS using a Vibroseis source are discussed by Miller et al. (2018). DAS specifications included calibration factors that converted field recorded raw data into physical units of nanostrain per second. The array recorded continuously. DAS data associated with the analysis of the Hawthorne earthquake are available at the National Geothermal Data Repository (University of Wisconsin, 2016a).

A conventional, 3-component array of 238 Fairfield Nodal ZLand 3C seismometers also recorded continuously. Seismometers were buried in shallow holes at a nominal depth of 0.3 m. Nodal specifications included calibration factors that converted signal counts into physical units of micrometers per second. The Nodal Zland 3C has a natural frequency of 5 Hz and a documented frequency response,[1] which transforms phase and amplitude of coil-case velocity into ground velocity. At 5 Hz the phase response is 90° and it approaches polarity reversal (180°) at 0.1 Hz. The amplitude response decreases about 2 decades per decade of decrease in frequency between 5 Hz and 0.1 Hz. Nodal geophone data associated with the analysis of the Hawthorne earthquake are available at the National Geothermal Data Repository (University of Wisconsin, 2016b).

Both active source and ambient noise studies are underway for three-dimensional, tomographic imaging of the experimental volume to determine the ability of the DAS and/or seismometer arrays to image the experimental volume (Zeng et al., 2017b; Thurber et al., 2017; Matzel et al., 2017).

DAS Recording of Ground Motion

The ground-motion information contained in DAS data is examined in this paper in physically meaningful ways by analyzing them in conjunction with the data recorded by the geophone array. First, the physical quantity measured by DAS is described. Second, the basic signal-to-noise characteristics of DAS data are presented using the geophone results as a benchmark in both time and frequency domain. Then, several physically based relationships between DAS data and co-located geophone data are examined using different cable segments.

DAS Strain-Rate Data

Silixa's DAS technology records ground motion as strain rate, $\dot{\varepsilon}$, measured in the direction of the cable (Parker et al., 2014; Daley et al., 2015). Light pulses (typically 50-100 nsec long) are sent into the fiber at a rate that is typically one pulse every 100 microseconds, i.e., at a frequency of 10 kHz. At each spatial sampling location x (channel) and at each time t, the Silixa DAS interrogator passes the backscattered light over a fixed distance (gauge length) L centered at x through optical components that create a coherent interference signal. The change in optical

[1] Zland 3C reference sheet: http://static.fairfieldnodal.com/assets/media/pdf/ZLand-3C-typical-specs.pdf and PASSCAL Instrument Center: https://www.passcal.nmt.edu/content/fairfieldnodal-zland-3-channel-sensor.

phase at each channel between successive pulses is computed and represents an accurate proxy for change in average optical length of a gauge-length segment of fiber, centered at the corresponding channel location. The data for our survey were calibrated in physical units by a gain of 11.6 nanometers per radian of optical phase change to obtain the change in displacement *u* between pulses over the gauge length *L* between time steps *t* and *t* + *dt* (Daley et al., 2015).

$$\left[u\left(x+\frac{L}{2},t+dt\right)-u\left(x-\frac{L}{2},t+dt\right)\right]-\left[u\left(x+\frac{L}{2},t\right)-u\left(x-\frac{L}{2},t\right)\right]. \quad (1)$$

Dividing by *L* and *dt* gives fiber strain-rate averaged over the gauge length. The gauge length sets the spatial resolution of the DAS array, which was 10 m in the PoroTomo survey. Typical value ranges from 7 to 35 meters (Mateeva et al., 2014). In theory longer gauge lengths should lead to higher SNR but lower spatial resolution. The spatial resolution is distinct from the spatial sampling, which may be as small as 0.25 meters (Miller et al., 2016) because Silixa's acquisition system oversamples both spatially and temporally to provide denoised raw files (see Daley, et al., 2015 for a detailed discussion of the optical noise).

The Brady strain-rate data were provided as a two-dimensional array at 1-m spacing between channels and 1 msec in time. The general practice of time integration was adopted to convert strain rate $\dot{\varepsilon}$ to cumulative strain ε. This processing step reduced optical noise. Because strain rate or strain is measured in the direction of cable, its amplitude decreases theoretically as $\cos^2\alpha$ ("broadside effect") (Mateeva et al., 2014), where α is the angle between the orientation of the cable and direction of earth particle motion for a perfectly coupled incident homogeneous compressional signal.

The DAS fiber cable in the Brady field is laid out in a zigzag pattern with 71 contiguous segments. To map the locations of the DAS channels, "tap" testing was performed at corners of the cable layout. The channel number associated with a sharp tap response was combined with its location by real-time GPS to provide a fiducial point identifying a specific cable channel with its UTM coordinates. Channels between tap-test locations were interpolated. Because channels within ten meters of a corner in the cable layout are influenced by the changing directional sensitivity, they are excluded from analyses that assume a constant direction for a cable segment.

The DAS data were stored in contiguous 30-second files in SEG-Y format. The delivered result of Silixa's processing of raw field data at the Brady site was about 45 terabytes of data.

Signal-to-Noise Ratio

An overview of the signal-to-noise ratio (SNR) characteristics of DAS data in the time domain is shown in Fig.3 for a four-second window around the P-wave arrival from the Hawthorne earthquake. Traces from Segments 60 through 71 comprise channels 6994 through 8671. We estimate the earthquake Signal-to-Noise Ratio (SNR) by comparing root-mean-square (RMS) amplitudes in representative one-second windows before and immediately following the P arrival. For the raw strain-rate data (Fig. 3b), this computation gives signal RMS = 0.40 με/sec, noise RMS = 0.09 με/sec, and an SNR = 4.4 or 13 dB. Because the raw signal is derived from optical interferometry, there is a small sensitivity to vibration of the interrogator that results in an easily estimated common signal present on all the DAS traces. After time-integration, which removes the interrogator system's photonic noise, and rejection of the common signal associated with interrogator shake, the data accurately represent a running 10-m average of fiber strain (Fig. 3c). For the fiber strain, signal RMS = 6.9 nε, noise RMS = 0.23 nε, and an SNR =30 or 30 dB, a significant improvement over the strain-rate SNR. As is evident in Fig. 3c, the noise in the strain signal consists substantially of heterogeneous propagating environmental signal. The earthquake arrival is similarly affected both by heterogeneity of the arriving signal and heterogeneity of the coupling to fiber strain, particularly at the corners of the zigzag deployment.

Next, we compared the signal-to-noise ratio (SNR) characteristics of several co-located DAS channels and Nodal geophones. In order to compare the same component of horizontal ground motion as DAS, the waveforms of the two horizontal components of a geophone were rotated into the direction of cable. A representative comparison is shown in Fig. 4 for Nodal geophone N131 and DAS channel CH346 in the southwestern part of the array at local coordinates X = 156.5 m; Y = -1.6 m in Fig. 1. The incident arrival from the M_L 4.3 Hawthorne earthquake is at an angle of ~35° relative to the orientation of the DAS cable segment, which is parallel to the X-axis. The noise window ('Noise' in Fig. 4) was defined to be a two-second-long interval before the P-wave arrival. The P and S windows were also chosen to be 2-second intervals after their respective arrivals. The time-domain SNR is defined to be the ratio between the maximum absolute value and the root-mean-square scatter during the noise window. For comparing the SNR obtained for different DAS channels and nearby geophones, we accounted for the angle α between the particle direction of the incident signal and the cable direction. The DAS strain is proportional to $\cos^2\alpha$, whereas the geophone velocity is linearly proportional to cos α. A preliminary beamforming analysis using the geophone array indicated that the incident angles of P and S waves are only a few degrees from the back azimuth to the earthquake. For CH346 the SNR uncorrected for angle α was 13 for the P wave and it was 37 for the S wave. Dividing by $\cos^2\alpha$ and cos α for DAS and geophone, respectively, the corrected SNRs were 21 and 58, respectively. For N131 the P-wave SNR uncorrected for angle α was 22 and the S-wave SNR was 94. The corrected SNRs were 27 and 117, respectively. Based on several dozen other comparisons, the time-domain P-arrival SNRs for geophone records ranged for the most part between 0.2 and 2 times the time-domain SNR of co-located DAS records (Fig. 5a). Although the range of SNRs was similar for the time-domain S-arrival, a significant number of geophone SNRs were greater than twice DAS SNRs (Fig. 5b), which may be related to the direction of the S-wave polarization.

Because of the frequency-dependent response of seismometers and DAS, the SNR is also frequency-dependent as discussed by Daley et al. (2015). Therefore, we also computed a frequency-domain SNR after obtaining the power spectral density (PSD) of noise and signal as a function of frequency using Welch's (1967) method. The left side of Fig. 6 shows spectrograms for the 50-second windows recorded by Nodal N131 and DAS CH346 that were shown in Fig. 4. The frequency content of the waveforms of the two sensors are remarkably similar as a function of time. The right side of Fig. 6 shows the power spectra for the two-second noise, P-arrival, and S-arrival windows. The P- and S-wave spectra contain more energy below 10 Hz than at higher frequencies where all three spectra converge.

The frequency-domain SNR was defined to be the power ratio at a given frequency. A comparison for the same example shown in Fig. 4 for the time domain SNR is shown in Fig. 7 for the frequency domain SNR. The frequency-domain SNRs of DAS and the geophone are very similar. The SNRs measured for the Hawthorne earthquake at Brady were better than those Daley et al. (2015) observed for active sources. In their study, they employed datasets from an active-sweep source to compare the quality of geophone and DAS records. After stacking they investigated the SNR of DAS to geophones with the result that DAS SNR was 18-to-24 dB lower. Compared with active sources, an earthquake signal contains more low frequency energy

This is a pre-copyedited, author-produced PDF of an article accepted for publication in Geophysical Journal International following peer review.
The version of record [Published 17 March 2018] is available online at: https://doi.org/10.1093/gji/ggy102

and the noise level is much lower at those lower frequencies (Fig. 7). Therefore, the SNR in our case is better even without any stacking.

The quality of DAS sensitivity to ground motion at the approximately 1-Hz frequency signal present in recordings of regional earthquakes is shown in Fig. 8. Two low-pass filters with cut-off frequencies of 1.0 and 0.5 Hz were applied to the raw data of co-located DAS channel 0346 and geophone N131. The results show that comparable P- and S-wave signals were recorded at frequencies down to 0.5 Hz (Fig. 8).

DAS Strain Rate as Finite Difference of Geophone Particle Velocities

Strain rate is defined mathematically by

$$\dot{\varepsilon} = \frac{\partial \varepsilon}{\partial t} = \frac{\partial}{\partial t}\left(\frac{\partial u}{\partial x}\right), \tag{2}$$

where *u* is the particle displacement in the cable direction *x*. The definition of strain rate in Eqn. (2) combined with the fact that DAS measures the average strain rate over the gauge length, *L*, leads to a finite difference relationship between strain rate as measured by a DAS channel and particle velocity as measured by a geophone.

$$\dot{\varepsilon}_{DAS}(x) = \frac{1}{L}\int_{x-\frac{L}{2}}^{x+\frac{L}{2}} \dot{\varepsilon}(l)dl = \frac{1}{L}\int_{x-\frac{L}{2}}^{x+\frac{L}{2}} \frac{\partial}{\partial t}\frac{\partial u}{\partial l}dl = \frac{1}{L}\int_{x-\frac{L}{2}}^{x+\frac{L}{2}} \frac{\partial}{\partial l}\frac{\partial u}{\partial t}dl = \frac{\dot{u}\left(x+\frac{L}{2}\right) - \dot{u}\left(x-\frac{L}{2}\right)}{L} \quad . \tag{3}$$

This relationship was derived by Bakku (2015) for a plane acoustic wave propagating along the fiber-optic cable. Eqn. (3) carries assumptions of a homogeneous medium and long wavelengths with respect to the gauge length. Eqn. (3) states that the DAS-measured strain rate is the finite difference of the particle velocity that is recorded one-half gauge length on either side of the DAS channel (Fig. 9 (top)). In other words, if there are two geophones whose compensated records represent particle velocity, the strain rate recorded by a DAS channel at the midpoint of the cable segment between them equals the difference of the two (velocity) seismograms divided by their separation distance. Eqn. (3) can be generalized to any pair of geophones spaced an integer number of gauge lengths apart by repeatedly summing channels one gauge length apart.

This is a pre-copyedited, author-produced PDF of an article accepted for publication in Geophysical Journal International following peer review.
The version of record [Published 17 March 2018] is available online at: https://doi.org/10.1093/gji/ggy102

For example, if there are four geophones and three DAS channels, the sum of three DAS channels at x = -L, 0, and +L is equal to the difference of geophones at x = +3L/2 and -3L/2 divided by L (Fig. 9 (bottom)). The intermediate geophones at x = -L/2 and L/2 cancel out.

$$\dot{\varepsilon}(-L)+\dot{\varepsilon}(0)+\dot{\varepsilon}(L)=\frac{\dot{u}\left(-\frac{L}{2}\right)-\dot{u}\left(-\frac{3L}{2}\right)}{L}+\frac{\dot{u}\left(\frac{L}{2}\right)-\dot{u}\left(-\frac{L}{2}\right)}{L}+\frac{\dot{u}\left(\frac{3L}{2}\right)-\dot{u}\left(\frac{L}{2}\right)}{L} =\frac{\dot{u}\left(\frac{3L}{2}\right)-\dot{u}\left(-\frac{3L}{2}\right)}{L}\,. \qquad (4)$$

In general, the summation leads to cancellation of terms representing interior geophones leaving only the difference of geophones at the end of a line segment of length nL when the seismic wavelength is much larger than the length of the line segment.

$$\dot{\varepsilon}\left[-\frac{(n-1)L}{2}\right]+\cdots+\dot{\varepsilon}[0]+\cdots+\dot{\varepsilon}\left[\frac{(n-1)L}{2}\right]=\frac{\dot{u}\left(\frac{nL}{2}\right)-\dot{u}\left(-\frac{nL}{2}\right)}{L}, \qquad (5)$$

The finite difference relationship Eqn. (5) between DAS strain rate and geophone particle velocity was tested along several cable segments (Fig. 10 (left)). Waveforms of the two horizontal geophone components were rotated into the direction of the fiber-optic cable to obtain the same component of ground motion as the DAS channels. The records of the DAS channels were converted to nanostrain per second using the calibration factor 11.6 nanostrain per radian supplied by Silixa. The first DAS channel used in Eqn. (5) is 5 m from the first geophone in the +x direction whereas the last channel is 5 m from the second geophone but in the –x direction. The interior channels used in Eqn. (5) were evenly sampled between the two ends in 10-channel (one, gauge length) steps (Fig. 10 (right)). The cable segment lengths vary from 20 to 100 meters; thus, the number of DAS channels in the summation in Eqn. (5) varies from 3 to 10. The angle between the cable segments and the incident wave from the Hawthorne epicenter varies between 13º and 67º.

For the comparisons, the raw waveforms obtained by the geophones were converted from counts to velocity seismograms in micrometers per second using the instrument calibration and frequency response information provided by Fairfield Nodal. Both DAS strain rate and geophone waveforms were bandpass filtered to select frequencies between 1 and 5 Hz. Because the shallow structures on the highway and hill sides (separated by a service road) are quite different (Zeng et al., 2017b), two series are shown for different cable segments to investigate possible effects of different incident wave azimuths and site conditions for DAS sensing versus geophones. Figs. 11 and 12 show the comparison of the left- and right-hand sides of Eqn. (5) for the configuration of geophones and DAS shown in Fig. 10 for the highway and hill side traces, respectively. Highway and hill side differences were not apparent. The plots include a time shift that maximizes absolute value of the cross-correlation coefficient between the two waveforms over the 50-second window. The time shift of 0.1 seconds or less includes effects from several factors. Although the timing of both acquisition systems was supposed to be synchronized via GPS, small time differences are still present. Second, the location of DAS cable is not exactly the same as the "co-located" geophone, which introduces an additional time difference. Third, the phase response of the geophone around the resonant/natural frequency is another factor that affects the waveform.

The left (DAS) and right (Nodals) hand sides of Eqn. (5) show high cross-correlation coefficients and very similar waveforms. The P- and S-wave arrivals appear distinctly for each sensor type. The amplitudes for the first several cycles of the P waves are also approximately the same. The S-wave comparisons are poorer possibly due to interference from P-wave coda. The coda is associated with converted phases and locally scattered signals off small-scale heterogeneities near the surface. The coda might affect DAS differently than geophones because of differences in ground coupling. Although both the geophones and DAS cable are buried at similar depths of a few tenths of a meter, geophones are coupled with a single spike whereas DAS' 10-meter gauge length can be irregular due to heterogeneity of the backfill or near-surface alluvium. Thus, the two sensors represent different spatial samples of ground motion.

In summary, the raw waveforms of the Hawthorne earthquake recorded by DAS and geophones appear very similar (Fig. 4). They do, however, sense different physical variables, are coupled differently, and have different response functions. The Silixa DAS system is configured to measure strain rate with a gauge length of 10 meters. Integrating time samples readily converts strain rate to strain. Definitions of strain in terms of displacement led to a finite-difference type of relation between DAS strain and geophone particle velocity (Eqns. (3) – (5)). Testing the equation with calibrated DAS and co-located geophones produced similar amplitudes in many cases (Figs. 11 and 12), which is surprising given the obvious differences in how the two sensors are coupled to the ground. The reasonably good cycle-for-cycle amplitude match deteriorates a few cycles after an arrival, which is attributed to coda associated with near-surface scattering that dominates the noise.

DAS as Strain Meter and Virtual Geophone

The concept of DAS as virtual geophones is based on the proportionality between strain and particle velocity for a plane wave, where slowness is the constant of proportionality (Benioff, 1935). Benioff (1935) and Mikumo and Aki (1963) used it to obtain phase velocity of surface waves from teleseismic earthquakes using data from a station with a co-located strain meter and seismometer. Benioff's "linear strain seismograph" was a 20-meter rod that measured the relative displacement of two piers using an electromagnetic transducer. Its base line length is similar conceptually to gauge length in the DAS array, although its two-point coupling to the earth is different than the continuous coupling of DAS cable buried in a shallow trench.

Relationship between Strain and Particle Velocity

The strain-particle velocity relationship was presented in the context of DAS by Daley et al. (2015) and Bakku (2015). For a plane wave propagating in the x-direction, $u(x,t) = A(x)e^{i(kx-\omega t)}$. Assuming $A(x)$ is constant,

$$\epsilon = \frac{\partial u}{\partial x} = \pm\frac{1}{c}\frac{\partial u}{\partial t} = \pm\frac{1}{c}\dot{u}, \qquad (6)$$

where $1/c = k/\omega$ is the apparent slowness in the cable direction (also assumed to be constant), $\dot{u} = \partial u/\partial t$ is particle velocity as measured by a conventional seismometer, and the sign is positive when the cable channel number increases in the direction of wave propagation. Eqn. (6) will serve as the initial basis for comparing a DAS channel with a co-located geophone. The proportionality constant $1/c$ can be obtained using a phase velocity obtained from moveout in the time domain from traces recorded in a DAS cable segment. Alternatively, it can be obtained as the ratio k/ω in the frequency-wavenumber (*f-k*) domain. The time domain approach will be used to convert a Nodal geophone trace to strain and the *f-k* domain approach will be used to convert a DAS channel trace to particle velocity. The comparisons will be limited by how the physical coupling of each sensor to the subsurface affects its recording of ground motion.

Converting Particle Velocity to Strain using Time-Domain Moveout

The apparent slowness is obtained in the time domain by tracking arrivals of a coherent phase of the P-wave arrival from the Hawthorne earthquake along a DAS cable segment. The locations of three geophones co-located with a DAS cable segment were chosen for the test are shown in Fig. 13. The cable segments ranged between about 50 and 200 meters in length. The apparent P-wave phase velocities ranged between 1124 and 1450 m/s from the best-fitting slopes obtained from the moveouts shown in Fig. 14. The apparent P-wave phase velocity is mainly controlled by two factors: P-wave velocity and incident direction. The V_P in the top 50 meters obtained from tomography is about 1300 m/s (Thurber et al., 2017), but strong heterogeneity is also present. The lower frequency of an earthquake arrival might also introduce uncertainty into picking the arrival. As was done in the previous section, the co-located DAS channel and geophone traces on a cable segment were bandpass filtered between 1 and 5 Hz after conversion from raw data to physical units. The time-domain moveout velocities were used to scale the Nodal traces (compensated for instrument response) and convert them to equivalent strain via Eqn. (6). The resulting comparisons between the three co-located DAS channels and geophones are shown in terms of strain for the P-wave arrival in Fig. 15 and for the S-wave arrival in Fig. 16. Although two of the three examples for each phase show comparable waveforms, the results are poorer visually and have lower cross-correlation coefficients than examples of the finite difference comparisons based on Eqn. (5) (Figs. 11 and 12). Given the small number of examples, no correlation could be made between the fit and the spatial location (highway side or hill side) of the cable segment.

We suspect that variable coupling along the cable segment adjacent to the co-located geophone may be responsible for the poorer match, although variable coupling should also play a role in the DAS-geophone comparison based on Eqn. (5). Controlled tests in uniform medium with uniform coupling are needed to investigate Eqns. (5) and (6) rigorously.

Converting Strain Rate to Particle Velocity in *f-k* Domain

DAS strain-rate data can also be converted to particle velocity by processing a cable segment in the *f-k* domain. As in the previous section, the raw DAS data were first converted to strain by integrating with respect to time. The strain waveforms were then Fourier-transformed in two dimensions from the time-space domain to the *f-k* domain. The transform coefficients $A(k,\omega)$ were scaled by k/ω because multiplication by k is equivalent to integration with respect to the spatial variable x and division by ω is equivalent to differentiation with respect to the time variable t. Thus, integrating strain with respect to x converts it to displacement and differentiating the result with respect to time converts it to particle velocity (Eqn. (2)). Therefore, we obtain particle velocity for each channel when $(k/\omega)\cdot A(k,\omega)$ is inversely transformed back to the time-space domain. Note that the procedure scales the Fourier coefficients $A(k,\omega)$ by the slowness k/ω, which is summarized below as MATLAB pseudo-script.

$$\dot{u} = ifft2((k/\omega)A(k,\omega)) . \quad (7a)$$

where $A(k,\omega) = fft2(\varepsilon(x,t))$. (7b)

The particle-velocity waveforms calculated by Eqn. (7) from a DAS cable segment can then be used to compare co-located DAS channels and geophones (compensated for instrument response and rotated into the cable direction) directly. Eqn. (7) converts a DAS channel into a "virtual geophone."

Out of 54 co-located pairs of DAS and geophones, we chose 6 to compare particle velocities calculated from Eqn. (7) with those obtained from geophones (Fig. 17). The comparisons span the whole array. Because the noise level is much lower below 5 Hz, all waveforms were band-pass filtered between 1 and 5 Hz. Two series of examples are shown: three pairs on the hill side (Fig. 18), and three pairs on the highway side (Fig.19). The DAS waveform has been transformed to a particle velocity using the *f-k* transform described by Eqn. (7) and the geophone waveform is scaled by dividing by the ratio of the root-mean-square amplitude of the geophone trace to that of the DAS trace (G/D in the left panel). As with the comparisons of DAS and geophones in the previous section, time-shifted cross-correlation was used to optimize the fit. The DAS virtual geophone and geophone waveforms fit each other well for the first couple of cycles in both the P and S windows. As with the DAS and geophone comparison of Eqn. (5), converted phases and locally scattered signals due to small-scale heterogeneity near the surface might lead to differences in the P-wave coda recorded by DAS with its 10-meter spatial averaging and geophones with their point coupling. Generally speaking, *f-k* scaling did not improve the waveform fit over the direct comparison of DAS strain versus a co-located geophone's particle velocity. Sometimes *f-k* scaling introduced a phase shift (e.g., N060), which might be due to changes in coupling along a cable segment.

In summary, a DAS cable segment can be used to convert its strain waveform into a particle-velocity waveform. Eqn. (7) was tested for the Brady array in two ways. In the time domain, apparent velocities, and hence, its reciprocal, slowness, were obtained by tracking the phase of an arrival along a cable segment. In the *f-k* domain, slowness was obtained using a cable segment for the 2-D Fourier transforms of Eqn. (7). The velocity or slowness was then used to scale the DAS strain rate for comparison with geophone particle-velocity waveforms (Figs. 15-16 and Figs. 18-19, respectively). The comparisons using calibrated values produced results significantly worse than tests of the finite difference Eqn. (5), as measured by cross correlation coefficients, although reasonably good matches were obtained for a couple of cycles after an arrival. One possible reason is that the coda can contain several superposed signals with different signs. The coda waves are associated with geologic heterogeneity, such as small scatterers (e.g. Poletto et al., 2016), which could affect the DAS waveform differently than a geophone's, because DAS spatially averages over 10 meters whereas the geophone is a point sensor.

Synthetic Strain Seismograms

Several synthetic strain seismograms were computed for the Hawthorne event to guide interpretation of the empirical observations. The University of Nevada, Reno (UNR) generates a list of moment tensor solutions using the using the inversion code of Ichinose et al. (2014). The code creates Green's functions for the available moment tensor solution (http://www.seismo.unr.edu/Earthquake accessed on 12/3/17) to compute displacement seismograms for any point in the region. The forward calculation used the 1-D Western US velocity model of Ritsema and Lay (1995). The displacement seismograms can then be rotated into the radial direction towards the earthquake epicenter and pairs of seismograms half a gauge length on either side of a DAS channel location can be differenced in space to yield strain du/dx.

Comparisons of DAS and geophone waveforms were made with synthetic strain seismograms for a segment of fiber that is approximately aligned with the back azimuth to the earthquake (Fig 20). Waveforms from four DAS channels were selected and integrated to yield strain. Also, waveforms from two geophones that are approximately co-located at the ends of the cable segment were rotated and integrated with respect to time to obtain displacement and differenced with respect to space to provide an alternate strain estimate. These are plotted together with the synthetic strain seismogram at the midpoint of the cable segment. As the synthetics are limited to a maximum frequency of about 0.5 Hz, due to the relatively simple model, and the geophone's corner frequency is 5 Hz, the strain waveforms derived from them were band passed from 0.25 to 0.5 Hz. Figure 20 shows the filtered results, which are trace-normalized and aligned by origin time.

The synthetic strain seismogram matches the geophone's well, except for the P wave, which is poorly recorded at these frequencies by the geophone, although evident at higher frequencies. The synthetics show a clear Rayleigh wave train about 60 seconds after the P, which is likely pronounced due to the simple velocity model, as more complex (and realistic) models tend to decrease the Rayleigh amplitude. The DAS signals resemble the synthetics for the channels at the ends of the cable segment; the P wave, in particular, is well matched. The slight difference in azimuth (< 20°) between the synthetics and the DAS does not have a significant effect on the seismograms.

Discussion

Both DAS and geophone arrays at Brady Hot Springs clearly recorded the regional $M_L = 4.3$ Hawthorne earthquake on March 21, 2016. Its epicenter was 150-kilometers SSE (159°) from the Brady natural laboratory. The co-located arrays provided the opportunity to compare the signal-to-noise characteristics of DAS and geophone data and to examine how their physical quantities are related to each other. These results provide insights into the potential for implementing DAS as a seismic array. A DAS array can contain a very large number of time-synchronous sensor points at meter-scale spatial density over distances that are tens of kilometers in length. DAS, however, records only a single component of strain and it is directionally sensitive. Theoretically, it has zero sensitivity to broadside motion. Lindsey et al. (2017) found that DAS

This is a pre-copyedited, author-produced PDF of an article accepted for publication in Geophysical Journal International following peer review.
The version of record [Published 17 March 2018] is available online at: https://doi.org/10.1093/gji/ggy102

and a broadband seismometer gave essentially identical estimates of main body wave arrival times, peak ground accelerations, and coda for a M3.8 Alaska Range earthquake recorded 150-km away in Fairbanks. They found as well that DAS did not record P-wave phases as well as the seismometer. Phase identification can be problematic using a single-component point sensor (Bormann et al., 2014), because polarization analysis, which is widely used to identify phase or to suppress noise (Schimmel and Gallart, 2003), cannot be used with DAS data. Other factors influence the earthquake waveforms recorded by a DAS array – optical system noise, signal and noise strengths and spectra, near-surface heterogeneity, and coupling of ground motion with the cable. The influence of the near-field geology of the cable array is assessed by a map of time-domain SNRs (Fig. 21) in which every tenth DAS channel is represented by a dot and contours are based on the SNR of the east component of geophones. The correlation between the two values suggests that the SNR of DAS is controlled mostly by site effects. In general, the central part of the "PoroTomo Natural Lab" is a low-velocity zone on tomography slices (Thurber et al., 2017) and also shows low SNR. Another indicator of local heterogeneity was observed by Miller et al. (2018) in interpreting two Vertical Seismic Profiles (VSPs) in borehole 56-1 located in the southwest corner of the array (Fig. 1). Distinctly different statics corrections were required for two profiles in which one Vibroseis source was to the northeast by 260 m and the other source was 260 m to the southwest. Strong site effects dominated directional sensitivity as we found no correlation between cable direction and SNR (Fig. 22). The crosses denote the measured SNR of the P-wave, which would be expected to vary only as a function of $\cos^2\alpha$, if directional sensitivity were the only variable. All the P-wave SNRs should be a single value. However, the plot shows that the measured SNR fluctuates widely for channels on cable segments for which $\cos^2\alpha$ is constant, which could be the result of local heterogeneity or variable coupling of the cable to the ground. A best-fit linear regression of SNR versus $\cos^2\alpha$ (red line) shows that the deviations do not show any trend with broadside angle. Variable near-surface geology, variable coupling or the changing direction of cable segments reduce wavefield coherency across the array, but it appears that the first two possibilities dominate at the Brady site.

Conclusions

The performance of overlapping arrays of 8.7 km of DAS cable and 238 geophones was studied using P- and S-wave arrivals from a M_L = 4.3 earthquake whose epicenter was 150 km away. Both arrays showed highly similar waveform traces in recording P- and S-wave ground motion from the earthquake. The signal-to-noise ratio of DAS cumulative strain is improved over raw strain rate. The signal-to-noise ratio of a single DAS channel was generally lower by a factor of two when compared to geophones at earthquake body-wave frequencies of a few Hertz, but increases at lower frequencies. The signal-to-noise ratios of both DAS and geophones varied with local geological heterogeneity. The SNRs measured for the Hawthorne earthquake at Brady were better than observed for active sources.

A comparison of DAS strain waveform as a finite difference of two geophone waveforms worked well in several test cases. Also, the strain waveforms measured by DAS correlated well with particle-velocity waveforms measured by geophones for the first couple of cycles after an arrival. Apparent velocities were obtained both by analyzing DAS data in the time domain and in the *f-k* domain. The amplitudes of the strain waveforms computed from geophone waveforms were comparable to those of DAS waveforms, although the waveforms themselves showed variable cross-correlation values. Synthetic strain seismograms can be a useful tool to provide a controlled baseline for first-order comparisons. In general, the physics of ground motion measured by DAS and geophones were confirmed. DAS has significant potential for contributing to seismic array analysis of regional earthquakes.

Acknowledgments

We are extremely grateful to Fan-Chi Lin (University of Utah), Amanda Thomas (University of Oregon), and Marianne Karplus (University of Texas-El Paso) for contributing their Fairfield Nodal Zland 3-component sensors to our project. We thank Michelle Robertson (LBNL) and the T-REX crew; Joe Greer, Thomas Coleman and the Silixa team; John Akerley, Paul Spielman, Janice Lopeman and Ormat Technologies; Neal Lord; and the PoroTomo field deployment personnel.

The paper was greatly strengthened by thorough and thoughtful reviews by editor Martin Schimmel and reviewer Pavel Golikov.

The work presented herein was funded in part by the Office of Energy Efficiency and Renewable Energy (EERE), U.S. Department of Energy, under Award Number DE-EE0006760. X. Zeng was also partially supported by the Hundred Talents Program of the Chinese Academy of Sciences. R. Mellors' contribution was prepared by LLNL under contract DE-AC52-07NA27344R.

References

Ali, S. T., Akerley, J., Baluyut, E. C., Cardiff, M., Davatzes, N. C., Feigl, K. L., Foxall, W., Fratta, D., Mellors, R. J., Spielman, P., Wang, H. F. & Zemach, E., 2016. Time-series analysis of surface deformation at Brady Hot Springs geothermal field (Nevada) using interferometric synthetic aperture radar. Geothermics, **61**, 114-120.

Bakku S. K., 2015. Fracture Characterization from Seismic Measurements in a Borehole, PhD Thesis, Massachusetts Institute of Technology, MA, USA.

Benioff, H., 1935. A linear strain seismograph, *Bull. Seismol. Soc. Am.,* **25**, 283-309.

Bormann, P., Klinge, K., & Wendt, S., 2014: Data Analysis and Seismogram Interpretation, in Bormann, P. (Ed.), *New Manual of Seismological Observatory Practice 2 (NMSOP-2)*, Potsdam : Deutsches GeoForschungsZentrum GFZ, pp. 1—126. DOI: http://doi.org/10.2312/GFZ.NMSOP-2_ch11.

Castongia E., Wang H.F., Lord N., Fratta D., Mondanos M., & Chalari A., 2017. An Experimental Investigation of Distributed Acoustic Sensing (DAS) on Lake Ice, *Journal of Environmental and Engineering Geophysics*, **22**(2), 167-176.

Daley T. M., Freifeld B. M., Ajo-Franklin J., Dou S., Pevzner R., Shulakova V., Kashikar S., Miller D. E., Goetz J., Henninges J., & Lueth S., 2013. Field testing of fiber-optic Distributed Acoustic Sensing (DAS) for subsurface seismic monitoring, *The Leading Edge*, **32**(6), 699-706.

Daley T. M., Miller D. E., Dodds K., Cook P., & Freifeld B. M., 2015. Field testing of modular borehole monitoring with simultaneous distributed acoustic sensing and geophone vertical seismic profiles at Citronelle, Alabama, *Geophysical Prospecting*, **64**(5), 1318-1334.

Feigl, K. L., & PoroTomo Team (2017). Overview and Preliminary Results from the PoroTomo Project at Brady Hot Springs, Nevada: Poroelastic Tomography by Adjoint Inverse Modeling of Data from Seismology, Geodesy, and Hydrology. Geothermal, *Proceedings*, 42nd Stanford Geothermal Workshop, Stanford University, Stanford, CA. Stanford University, Stanford, California, February 13-15, 2017, SGP-TR-212, 15 pp.

Freifeld, B. M., Pevzner, R., Don, S., Correa, J., Daley, T. M., Robertson, M., Tertyshnikov, K., Wood, T., Ajo-Franklin, J., Urosevic, & M., Gurevich, B., 2016. The CO2CRC Otway Project deployment of an Areal Distributed Acoustic Sensing Network Coupled with Permanent Rotary Sources, *78th EAGE Conference & Exhibition 2016*, Vienna, Austria, 30 May – 2 June 2016.

Ichinose, G., Roman-Nieves, J. and G. Kraft., 2014. Moment Tensor Inversion Toolkit (MTINV) Documentation, Manual and Tutorial, http://crack.seismo.unr.edu/htdocs/students/Ichinose/mtinv/mtinv.pdf (accessed Dec. 12, 2018).

Johannessen K., Drakeley B., & Farhadiroushan M., 2012. Distributed Acoustic Sensing - a new way of listening to your well/reservoir, *SPE Intelligent Energy International* held in Utrecht, The Netherlands, 27–29 March 2012, SPE 149602, 9 pp.

Jolie, E., Moeck, I., & Faulds, J. E., 2015. Quantitative structural–geological exploration of fault-controlled geothermal systems-A case study from the Basin-and-Range Province, Nevada (USA), *Geothermics*, **54**, 54-67.

Lancelle C., Baldwin J. A., Lord N. E., Fratta D., Chalari A., & Wang H. F., 2017. Using Distributed Acoustic Sensing (DAS) for Multichannel Analysis of Surface Waves (MASW) to evaluate ground stiffness, *Near Surface Geophysics*, submitted.

Lim I., Ning C., & Sava, P., 2016. Multicomponent distributed acoustic sensing. *SEG Technical Program Expanded Abstracts 2016*, pp. 5597-5602. doi: 10.1190/segam2016-13952981.1

Madsen K.N., Dümmong S., Kritski A., Pedersen Å.S., Finfer D., Gillies A., & Travis P., 2013. Simultaneous Multiwell VSP in the North Sea Using Distributed Acoustic Sensing, *75th EAGE Conference & Exhibition incorporating SPE EUROPEC 2013*, London, UK, 10-13 June 2013, 5 pp.

Mateeva A., Lopez J., Potters H., Mestayer J., Cox B., Kiyashchenko D., Wills P., Grandi S., Hornman K., Kuvshinov B., Berlang W., Yang Z., & Detomo R., 2014. Distributed acoustic sensing for reservoir monitoring with vertical seismic profiling, *Geophysical Prospecting*, **62**, 679–692.

Matzel, E., Zeng, X., Thurber, C., Luo, Y., & Morency, C., 2017. Seismic Interferometry Using the Dense Array at the Brady Geothermal Field. *Proceedings*, 42nd Stanford Geothermal Workshop, Stanford University, Stanford, California, February 13-15, 2017, SGP-TR-212, 4 pp.

Mellors R. J., Pitarka A., Kuhn M., Stinson B., Ford S. R., Snelson C., & Drachenberg D., 2014. Fiber Optic Acoustic Sensing (FOAS) Far-Field Observations of SPE 3, *Seismological Research Letters*, 85(2), 450 (abstract).

Mikumo, T. & Aki, K., 1964. Determination of local phase velocity by intercomparison of seismograms from strain and pendulum instruments, *J. Geophys. Res.,* **69**, 721-731.

Miller D., Parker T., Kashikar S., Todorov M., & Bostick T., 2012. Vertical Seismic Profiling using a fibre-optic cable as a Distributed Acoustic Sensor, *74th EAGE Conference &*

Exhibition incorporating SPE EUROPEC 2012, Copenhagen, Denmark, 4-7 June 2012, 5 pp.

Miller D. E., Daley T. M., White D., Freifeld B. M., Robertson, M., Cocker, J., & Craven, M., 2016. Simultaneous Acquisition of Distributed Acoustic Sensing VSP with Multi-mode and Singlemode Fibre Optic Cables and 3C- Geophones at the Aquistore CO2 Storage Site, *CSEG* Recorder, June 2016, 28-33.

Miller, D.E, Coleman,T., Zeng, X., Patterson, J.R., Reinisch, E., Cardiff, M.A., Wang, H.F., Fratta, D., Trainor-Guitton, W., Thurber, C.H., Feigl, K., & the PoroTomo Team, DAS and DTS at Brady Hot Springs: Observations about coupling and coupled interpretations, *Proceedings*, 43rd Stanford Geothermal Workshop, Stanford University, Stanford, CA. Stanford University, Stanford, California, February 12-14, 2018.

Parker T., Shatalin S. V., & Farhadiroushan M., 2014. Distributed Acoustic Sensing - A new tool for seismic applications, *First Break*, **32**(2), 61-69.

Poletto, F., Finfer, D., Corubolo, P., & Farina, B., 2016. Dual wavefields from distributed acoustic sensing measurements, *Geophysics*, **81**(6), D585-D597.

Ritsema, J. & Lay, T., 1995. Long-period regional wave moment tensor inversion for earthquakes in the western United States, J. Geophys. Res., 100, 9853-9864.

Schimmel, M., & Gallart, J. (2003). The use of instantaneous polarization attributes for seismic signal detection and image enhancement. *Geophysical Journal International*, *155*(2), 653-668.

Siler D.L. & Faulds J.E., 2013. Three-Dimensional Geothermal Fairway Mapping: Examples From the Western Great Basin, USA, Geothermal Resources Council Transactions, 37, 327–332.

Thurber, C., Zeng, X., Parker, L., Lord, N., Fratta, D., Wang, H., Matzel, E., Robertson, M., Feigl, K., & PoroTomo Team, 2017. Imaging seismic structure of geothermal reservoir with large N array at Brady Hot Springs, Nevada, 2017 Annual meeting of Seismological Society of America, Denver, CO (abstract).

University of Wisconsin. (2016a). PoroTomo Project - Subtask 6.2: Deploy and Operate DAS and DTS arrays - DAS Earthquake Data [data set]. Retrieved from https://gdr.openei.org/submissions/848. https://dx.doi.org/10.15121/1334285.

University of Wisconsin. (2016b). PoroTomo Subtask 6.3 Nodal Seismometer Earthquake Data [data set]. Retrieved from https://gdr.openei.org/submissions/846. https://dx.doi.org/10.15121/1334284.

Wang, H.F., Zeng, X., Lord, N.E., Fratta, D., Coleman, T., MacLaughlin, M., 2017. Field trial of Distributed Acoustic Sensing in an active room-and-pillar mine, 2017 Fall meeting of American Geophysical Union, New Orleans, LA, 11-15 Dec. (abstract S33F-03).

Welch, P. D., 1967. The use of Fast Fourier Transform for the estimation of power spectra: A method based on time averaging over short, modified periodograms, *IEEE Transactions on Audio and Electroacoustics*, AU-15 (2), 70–73.

Yavuz S., Freifeld B. M., Pevzner R., Tertyshnikov K., Dzunic A., Ziramov S., Shulakova V., Robertson M., Daley T. M., Wood T., Kepic A., & Urosevic M., 2016. Kinmetrics EPI ES-T buried DAS and geophone arrays: preliminary results from CO2CRC Otway project, *78th EAGE Conference & Exhibition 2016*, Vienna, Austria, 30 May – 2 June 2016.

Zeng X., Lancelle, C. Thurber C., Fratta D., Wang H. F., Lord N., Chalari A., & Clarke A., 2017a. Properties of ambient noise cross-correlation functions obtained from a Distributed Acoustic Sensing array at Garner Valley, California, *Bull. Seismol. Soc. Am.*, **107**, 603-610.

Zeng, X., Thurber, C., Wang, H., Fratta, D., Matzel, E., & PoroTomo Team, 2017b. High-resolution Shallow Structure Revealed with Ambient Noise Tomography on a Dense Array. *Proceedings*, 42nd Stanford Geothermal Workshop, Stanford University, Stanford, California, February 13-15, 2017, SGP-TR-212, 5 pp.

Figure Captions

Figure 1. PoroTomo natural laboratory and DAS cable layout at Brady Hot Springs. The boundaries of the natural laboratory are shown as a grey rectangle. The surface DAS cable is shown by the blue line and geophones are denoted with crosses. The injection, production, and observation wells are indicated with red, blue, and green solid circles, respectively. A 340-m long DAS cable was installed in Well 56-1. Highway I-80 and service road are denoted with solid and dashed green lines, respectively.

Figure 2. Location of Hawthorne earthquake (M_L = 4.3, https://earthquake.usgs.gov/earthquakes/eventpage/nn00536374) 150-km south-southeast of Brady Hot Springs.

Figure 3. (a) DAS traces in (b) and (c) are for 12 cable segments shown in red on the cable map. Ray direction from Hawthorne earthquake is shown as blue arrow. (b) Raw DAS recording of strain rate. Time is seconds after origin time of M_L 4.3 Hawthorne earthquake. (c) Integration with respect to time of raw DAS from strain rate to strain. Noise and P-wave signals were averaged within the red boxes to obtain SNR of 4.4 for strain rate and 30 for strain.

Figure 4. Example comparison of normalized DAS strain rate (blue) and raw geophone coil-case velocity (red) records for March 21, 2016 Hawthorne earthquake. Boxes show the two-second time windows that were used to obtain noise and signal for P and S-wave arrivals. The geophone record was scaled to match its peak amplitude to that of DAS. The inset map shows location of DAS segment (red line) and geophone (green triangle).

Figure 5. Comparison of time domain SNR of P- (left) and S-wave (right) arrivals of co-located raw geophone coil-case velocity and raw efDAS strain rate records. Slopes of ½, 1, and 2 are shown for reference as dashed lines.

Figure 6. Spectrogram (left side) and power spectral densities (PSD) for P-wave and S-wave arrivals and noise for raw Geophone N131 coil-case velocity (top right) and raw DAS CH 346 strain rate (bottom right) records.

Figure 7. Comparison of frequency-domain SNR of P- (left) and S-(right) wave arrivals for raw Geophone N131 coil-case velocity (red) and raw DAS CH 346 strain rate (blue) records.

Figure 8. Comparison of DAS CH0346 strain rate (blue) and geophone N131 case coil (red) waveforms for raw and low-pass P- and S-waves cut off (lp c) at 0.5 and 1 Hz.

Figure 9. (Top) Illustration of Eqn. (3) for two geophones spaced 1-gauge-length L apart where a DAS channel located at the midpoint is the finite difference of a pair of geophones particle-velocity recordings. The triangles are geophones and the circle is a DAS channel; (Bottom) Illustration of Eqn. (4) for two geophones spaced 3-gauge-lengths apart in which case the sum of the three DAS channels is equal to the difference of the two geophones at the end of the segment divided by L.

Figure 10. (Left) Map showing locations of DAS cable segments (red) and geophone pairs used in Eqn. (5). The Hawthorne-to-Brady direction is shown as a black arrow. (Right) Geometry of each DAS cable segment and geophone pairs. The horizontal axis is distance along cable for each line segment.

Figure 11. Highway side test of Eqn. (5). Compensated geophone ground velocity (red) and DAS strain rate waveforms (blue) were bandpass filtered between 1 and 5 Hz and aligned using the best-fit, time-shifted cross correlation. Both P and S-wave arrivals are shown. On the left set of panels, the DAS and geophone waveforms have been offset vertically for clarity. The geophone waveform has been divided by gauge length L according to Eqn. (5) so that both plotted traces are in units of nanometers/second. The cross-correlation coefficient (CC) between the two waveforms and the angle between the DAS cable segment and earthquake arrival are shown. The middle column expands the time scale for the P-wave arrival and the right column expands the time scale for the S-wave arrival. (Top) Cable segment CH498- CH541, (Middle) Cable segment CH398 – CH441. (Bottom) Cable segment CH1761-CH1815.

Figure 12. Hill side test of Eqn. (5). Compensated geophone ground velocity (red) and DAS strain rate waveforms (blue) were bandpass filtered between 1 and 5 Hz and aligned using the best-fit, time-shifted cross correlation. Both P and S-wave arrivals are shown. See caption of Fig. 11 for details. (Top) Cable segment CH5434-5492. (Middle) Cable segment CH5900-CH5921. (Bottom) Cable segment CH7009-CH7102.

Figure 13. Three co-located DAS channels and geophones (red triangles) were compared using Eqn. (6). DAS cable is shown in green line.

Figure 14. The apparent velocities of the P-wave arrival measured from raw DAS strain rate traces along cable segments near the three geophones shown in Fig. 13. The gray-scale shading represents amplitude while three individual traces are shown in blue. The apparent velocities are obtained from the best-fit slopes shown by the red lines. (a) CH 0482 – 0688 is 1124 m/s. (b) CH 2068 – 2113 is 1452 m/s. (c) CH 8431 – 8643 is 1185 m/s.

Figure 15. Three P-arrival comparisons of co-located DAS channels (blue) and geophones (red) using Eqn. (6) and apparent velocities from Fig. 14. DAS traces are strain and geophone traces are ground velocity after compensating for instrument response. DAS and geophone traces were bandpass filtered between 1 and 5 Hz after conversion from raw data to physical units. The apparent velocities, ratios of RMS amplitudes, and cross-correlation coefficients of geophone and DAS signals are shown in upper left corner of each panel.

Fig. 16. Three S-arrival comparisons of co-located DAS channels (blue) and geophones (red) for P-wave arrival using Eqn. (6) and apparent velocities from moveout (not shown). DAS traces are strain and geophone traces are ground velocity after compensating for instrument response. DAS and geophone traces were bandpass filtered between 1 and 5 Hz after conversion from raw data to physical units. The apparent velocities, ratios of RMS amplitudes, and cross-correlation coefficients of geophone and DAS signals are shown in upper left corner of each panel.

Figure 17. Six co-located DAS channels and geophones (red triangles) were compared using Eqn. (7). DAS cable is shown in green line. The arrow is the direction of the incident wavefield from the Hawthorne earthquake.

Figure 18. Hill side test of Eqn. (7). Compensated geophone ground velocity (red) and DAS time-integrated strain waveforms (blue) were bandpass filtered between 1 and 5 Hz and aligned using the best-fit, time-shifted cross correlation. In the left column, the DAS and geophone waveforms have been offset vertically for clarity in the left set of panels. The middle column expands the time scale for the P-wave arrival and the right column expands the time scale for the S-wave arrival. (Top row) N026 and CH 5642. (Middle row) N049 and CH 5558. (Bottom row) N060 and CH 7107.

Figure 19. Highway side test of Eqn. (7). See caption of Fig. 18 for details. (Top row) N134 and CH 874. (Middle row) Cable segment N141 and CH 2417. (Bottom row) N147 and CH 3017.

Figure 20. Comparison of synthetic strain seismogram, DAS channels, and geophone finite difference.

Figure 21. Time-domain DAS and geophone SNR map for (a) P-wave arrival and (b) S-wave arrival. Dots are the SNR of every 10th DAS channel and contours are based on the SNR of the east component of geophones, which is a good approximation of site effects.

Figure 22. DAS P-wave SNR (crosses) versus $\cos^2\alpha$ (red line), which corrects for directional sensitivity. The absence of correlation with cable orientation relative to horizontal particle direction is evidence that site effects dominate the SNR.

Fig. 1

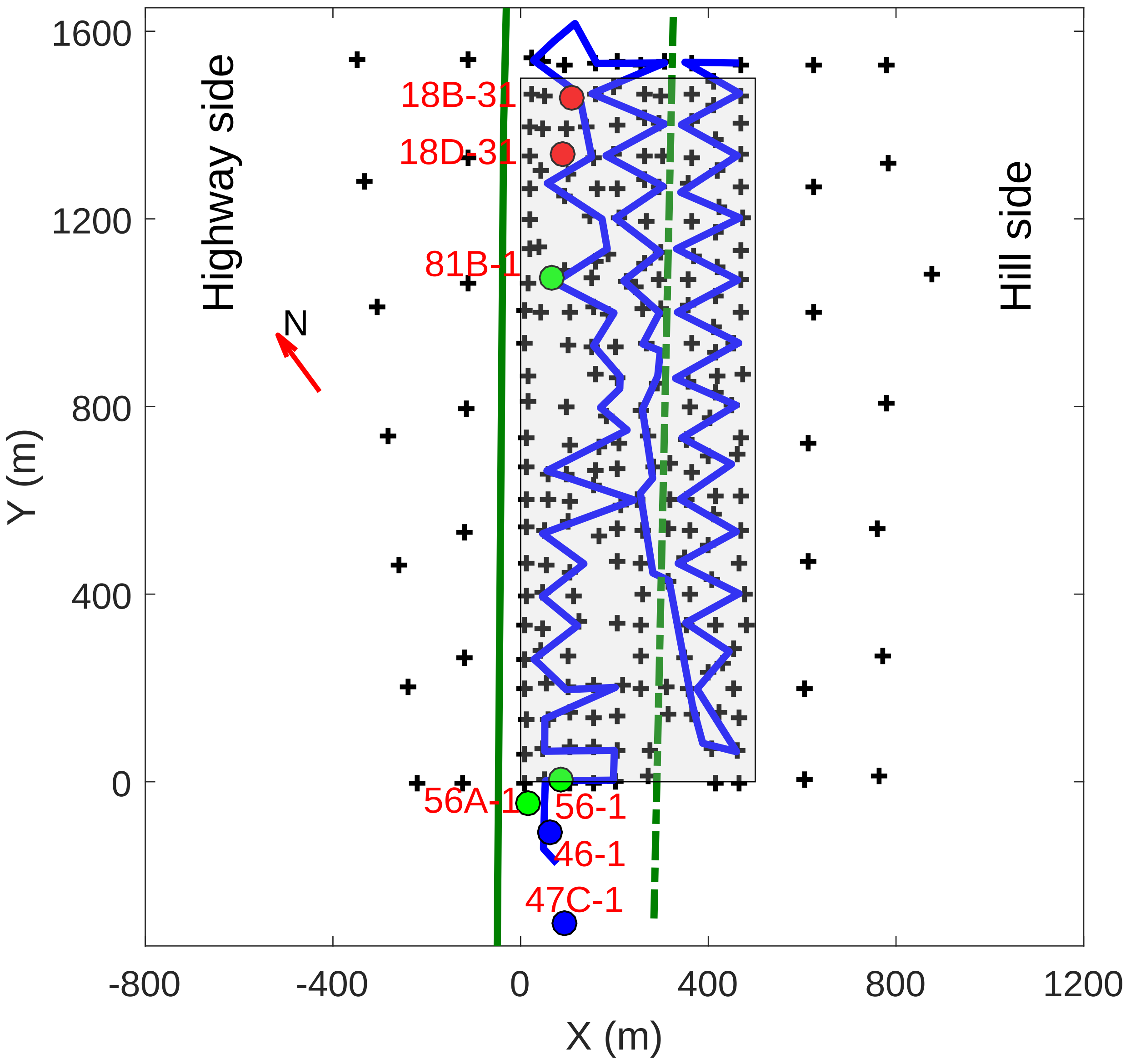

1600
1200
800
400
0
-800
-400
0
400
800
1200
Y (m)
X (m)
Highway side
Hill side
N
18B-31
18D-31
81B-1
56A-1
56-1
46-1
47C-1

Fig. 2

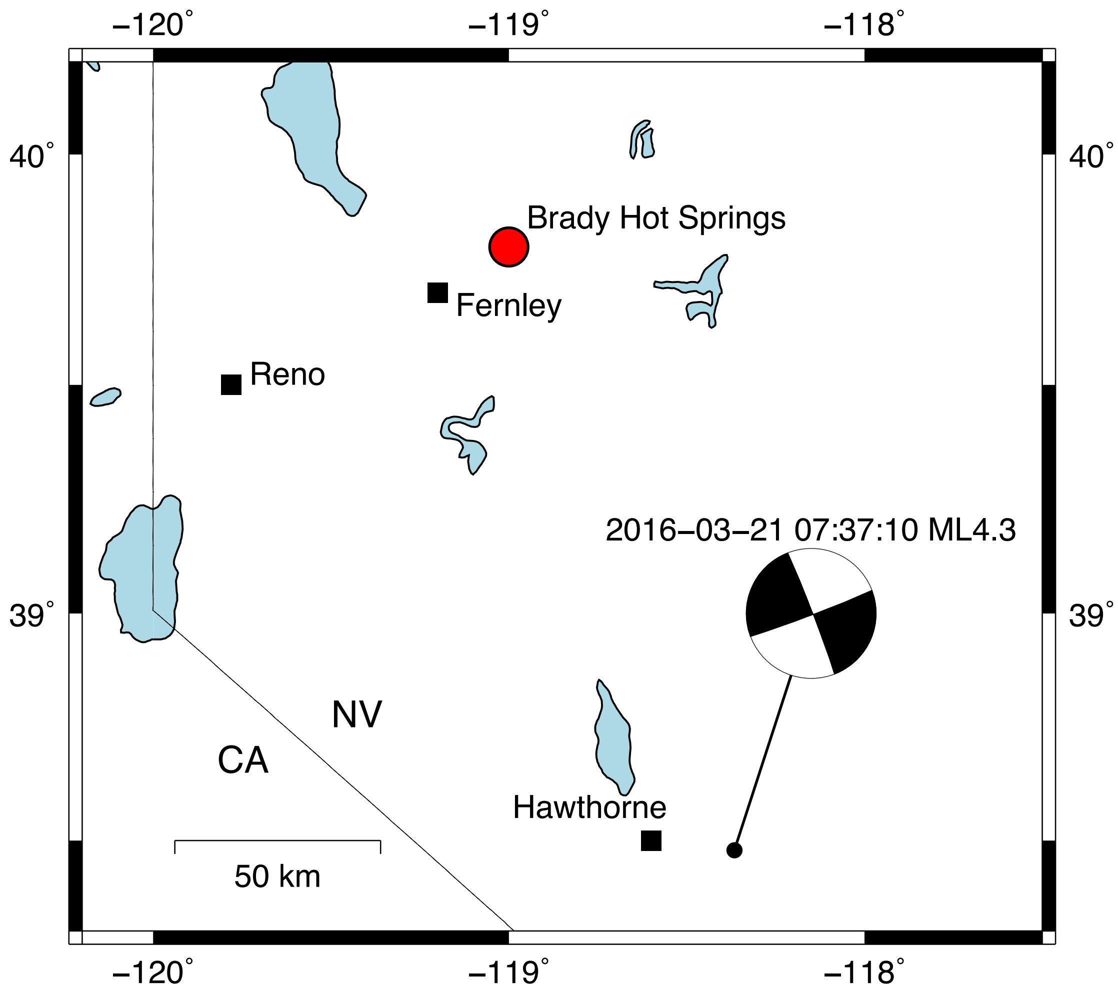
−120˚
−119˚
−118˚
40˚
39˚
Brady Hot Springs
Fernley
Reno
2016−03−21 07:37:10 ML4.3
NV
CA
Hawthorne
50 km

Fig. 3

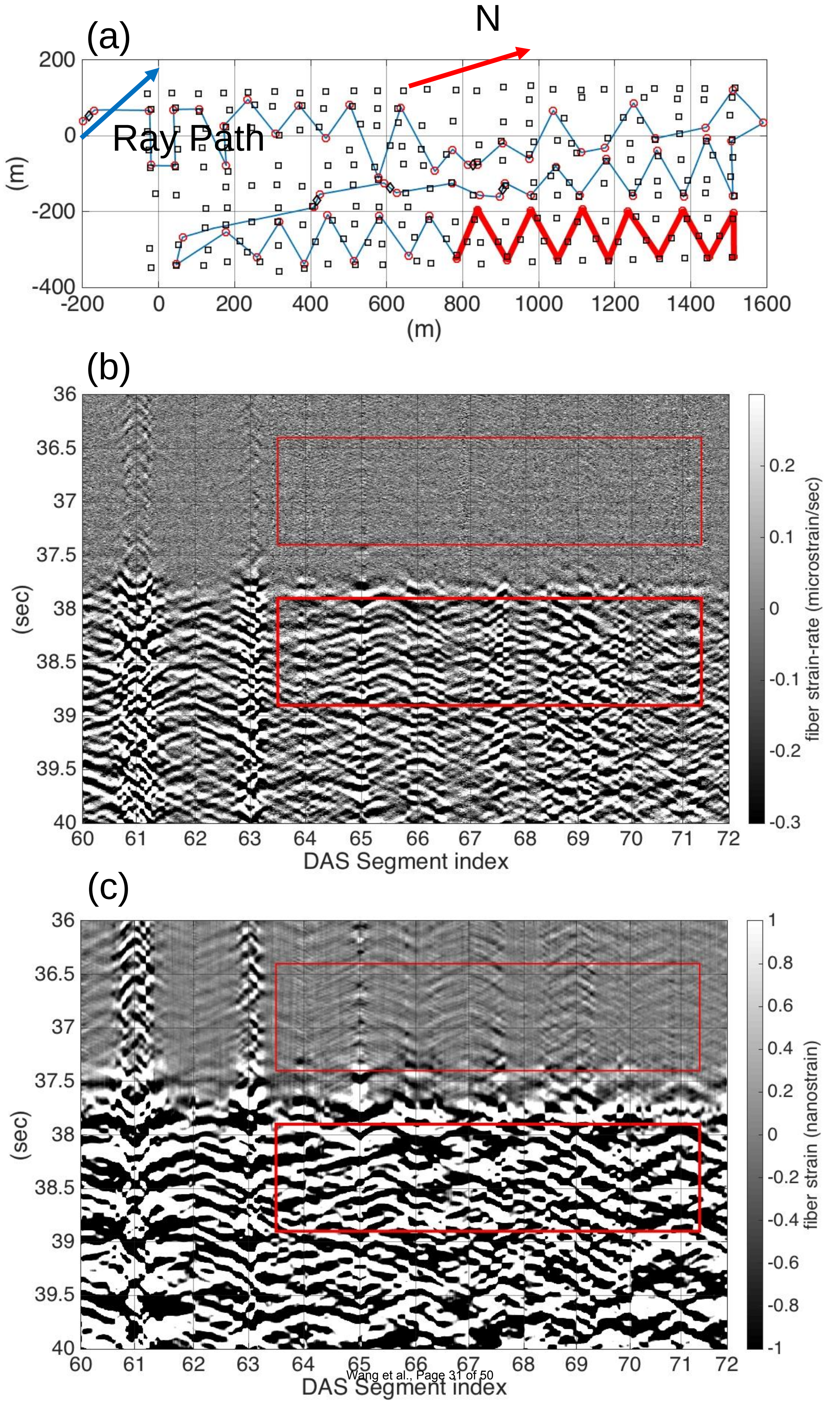
(a)
N
Ray Path
200
0
-200
-400
(m)
-200
0
200
400
600
800
1000
1200
1400
1600
(m)
(b)
36
36.5
37
37.5
38
38.5
39
39.5
40
(sec)
60
61
62
63
64
65
66
67
68
69
70
71
72
DAS Segment index
0.2
0.1
0
-0.1
-0.2
-0.3
fiber strain-rate (microstrain/sec)
(c)
36
36.5
37
37.5
38
38.5
39
39.5
40
(sec)
60
61
62
63
64
65
66
67
68
69
70
71
72
DAS Segment index
1
0.8
0.6
0.4
0.2
0
-0.2
-0.4
-0.6
-0.8
-1
fiber strain (nanostrain)

Fig. 4

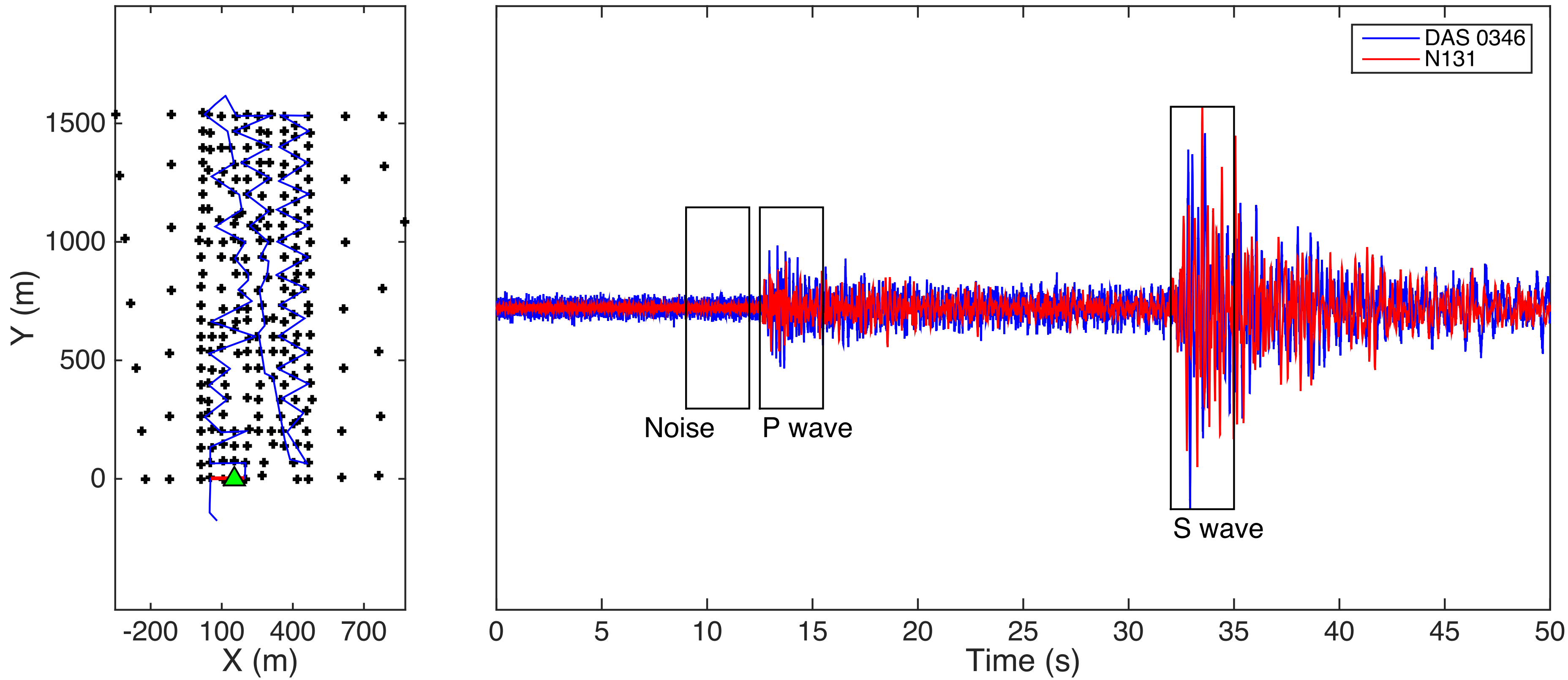
1500
1000
500
0
Y (m)
-200
100
400
700
X (m)
DAS 0346
N131
Noise
P wave
S wave
0
5
10
15
20
25
30
35
40
45
50
Time (s)

Fig. 5

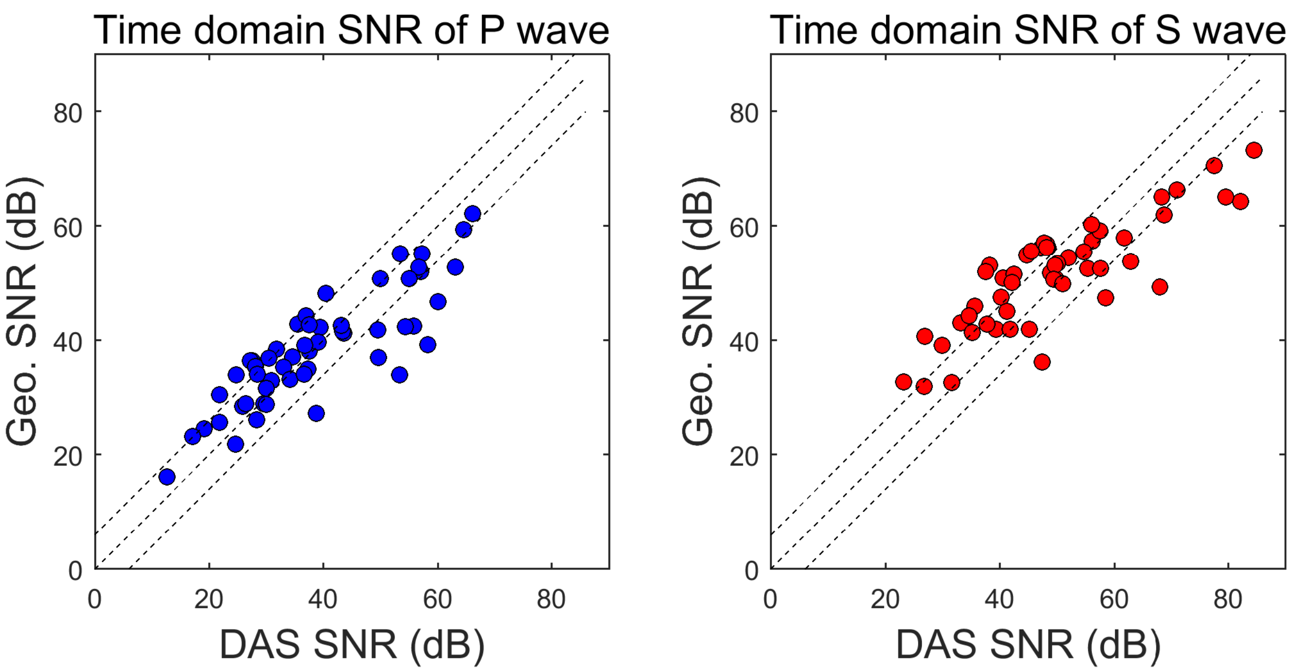
Time domain SNR of P wave
Geo. SNR (dB)
DAS SNR (dB)
0
20
40
60
80
Time domain SNR of S wave
Geo. SNR (dB)
DAS SNR (dB)

Fig. 6

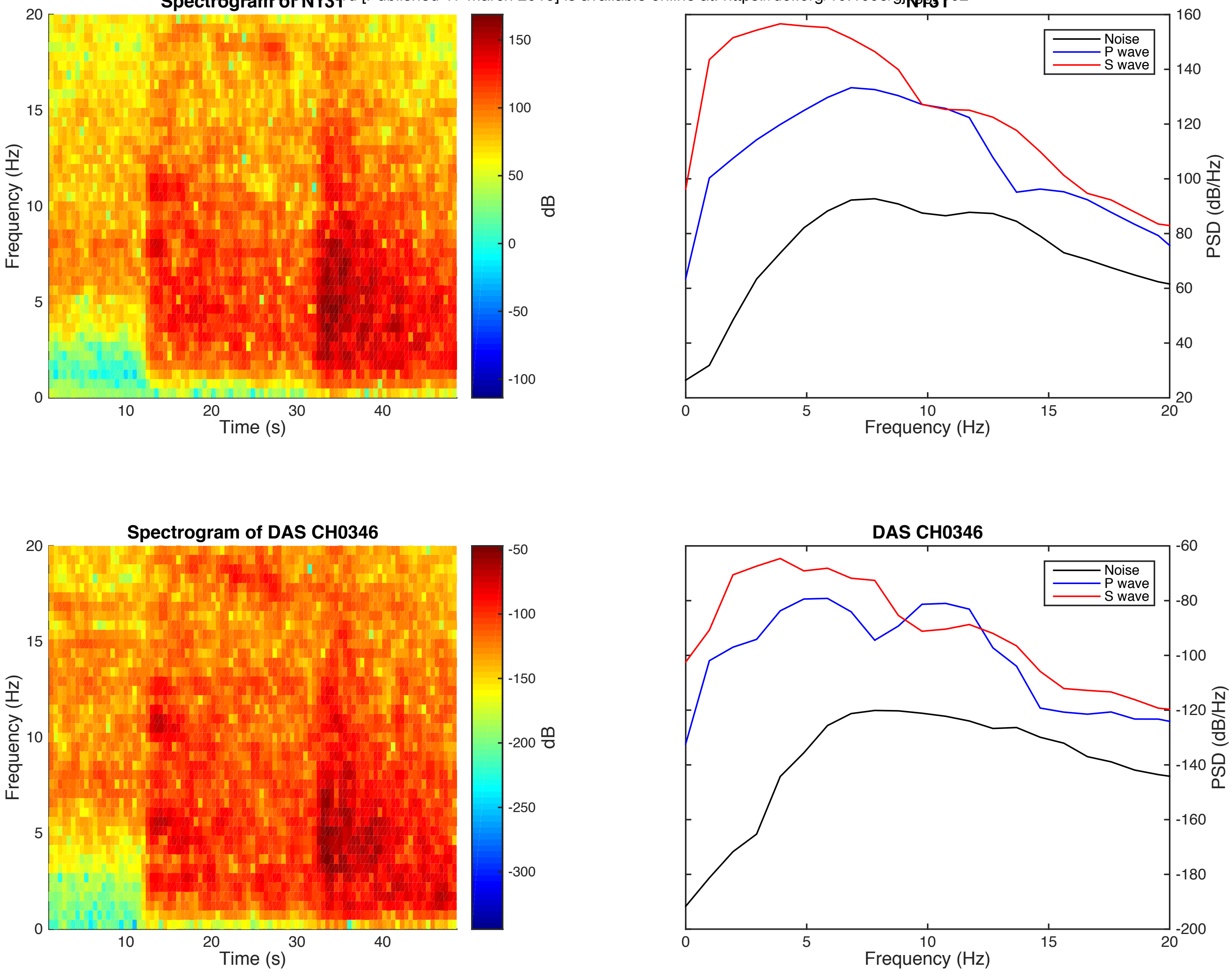
Spectrogram of N131
Frequency (Hz)
Time (s)
dB
N131
Noise
P wave
S wave
PSD (dB/Hz)
Frequency (Hz)
Spectrogram of DAS CH0346
Frequency (Hz)
Time (s)
dB
DAS CH0346
Noise
P wave
S wave
PSD (dB/Hz)
Frequency (Hz)

 Fig. 7

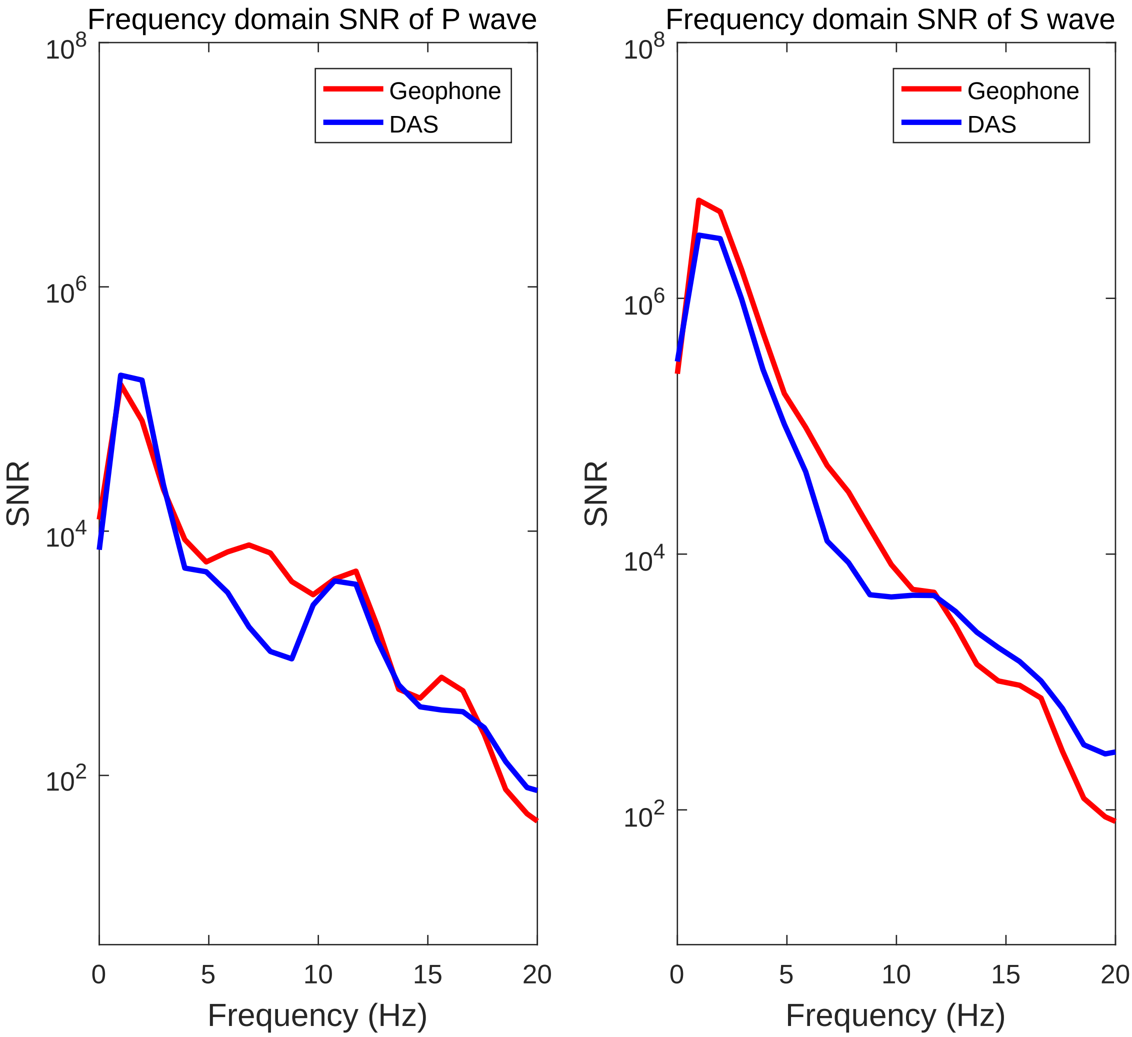
Frequency domain SNR of P wave
Geophone
DAS
SNR
10^8
10^6
10^4
10^2
0
5
10
15
20
Frequency (Hz)
Frequency domain SNR of S wave
Geophone
DAS
SNR
10^8
10^6
10^4
10^2
0
5
10
15
20
Frequency (Hz)

Fig. 8

This is a pre-copyedited, author-produced PDF of an article accepted for publication in Geophysical Journal International following peer review.
The version of record [Published 17 March 2018] is available online at: https://doi.org/10.1093/gji/ggy102

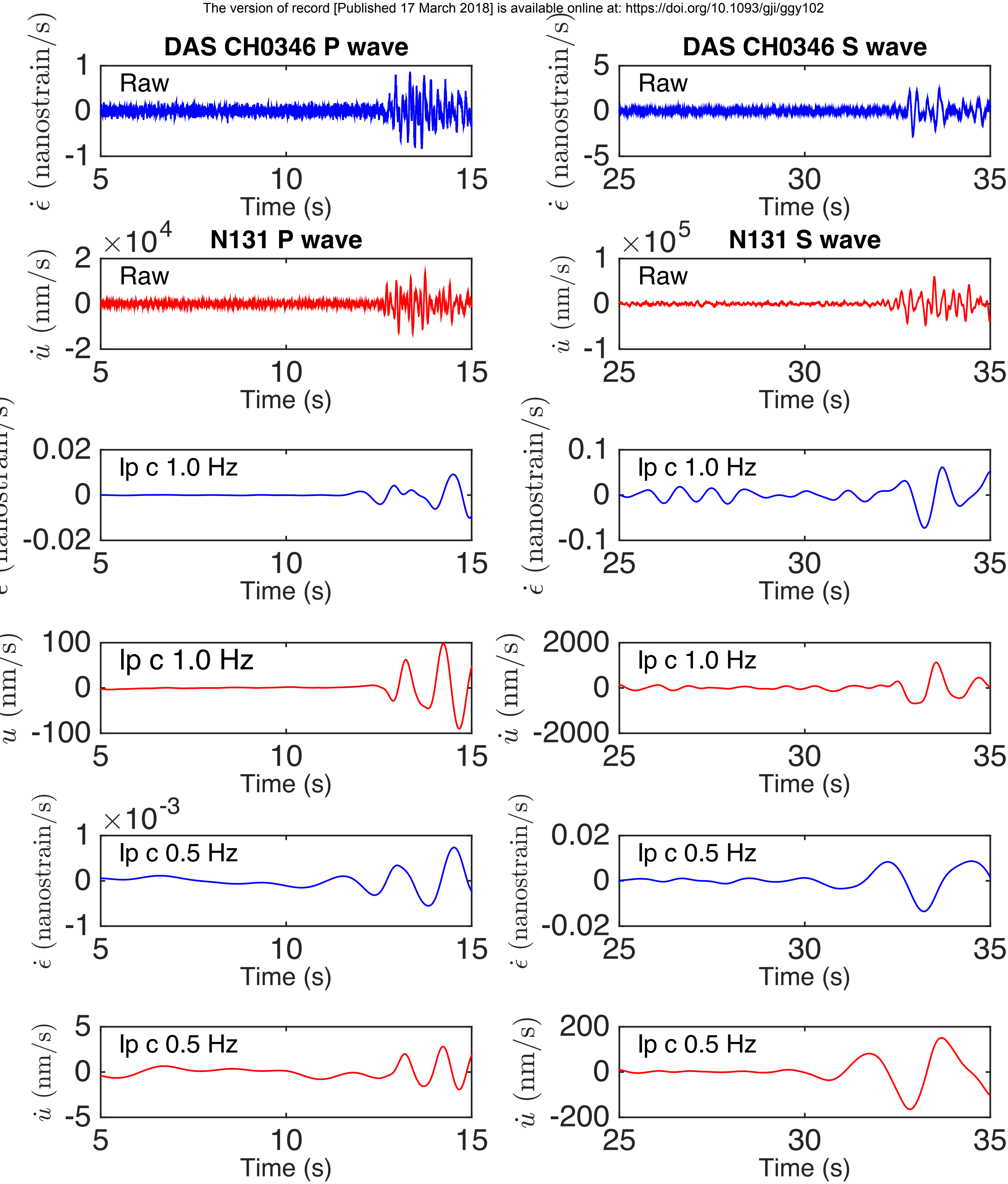

Fig. 9

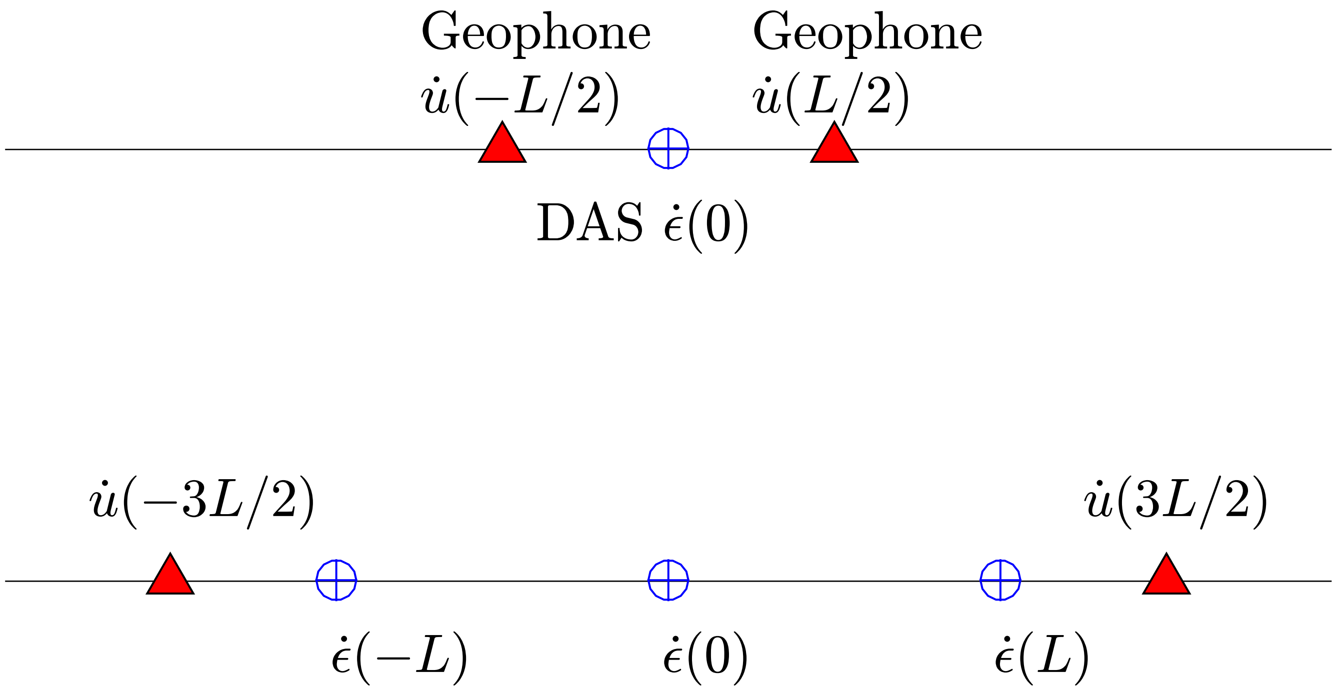
Geophone
$\dot{u}(-L/2)$
Geophone
$\dot{u}(L/2)$
DAS $\dot{\epsilon}(0)$
$\dot{u}(-3L/2)$
$\dot{u}(3L/2)$
$\dot{\epsilon}(-L)$
$\dot{\epsilon}(0)$
$\dot{\epsilon}(L)$

Fig. 10

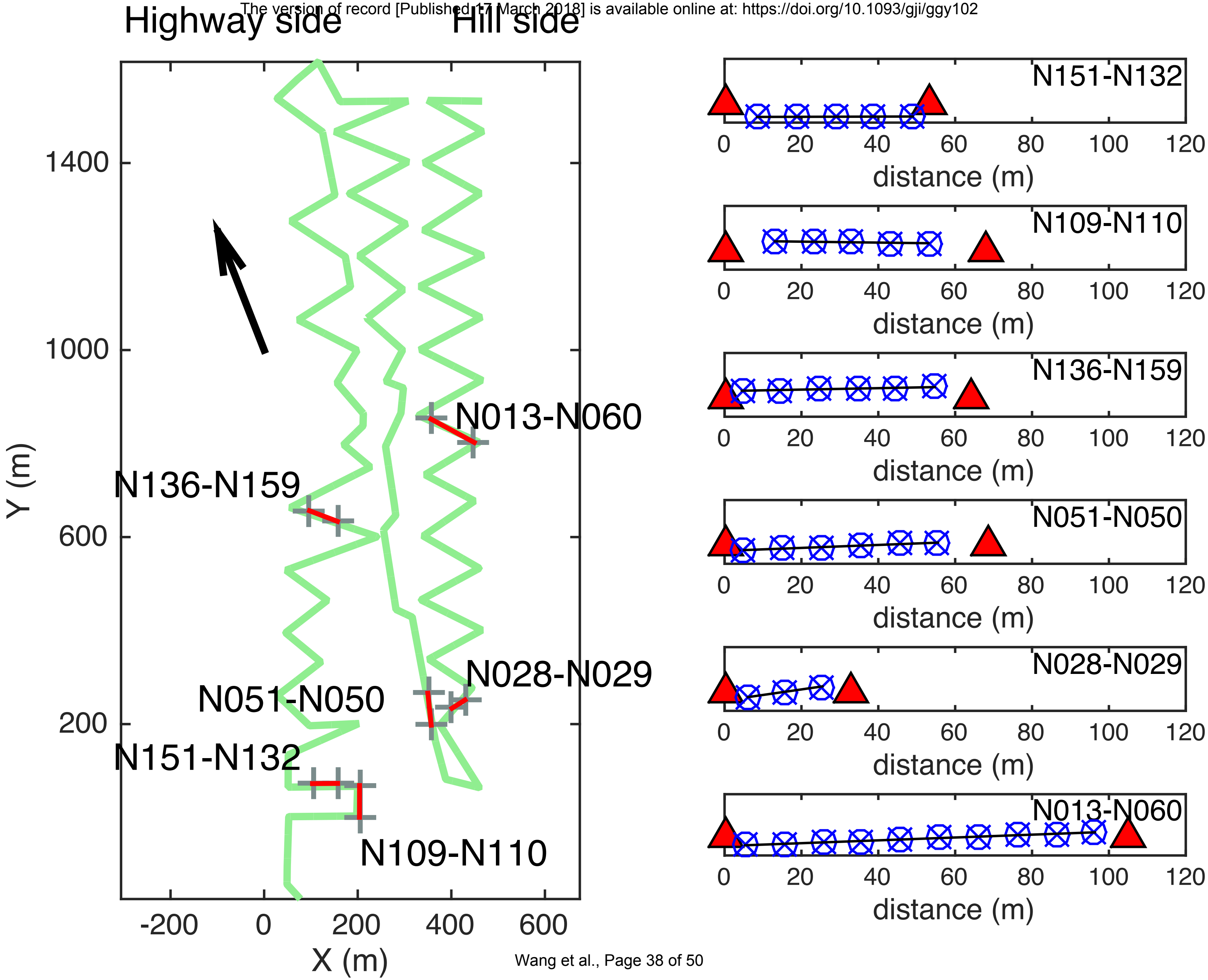
Highway side
Hill side
1400
1000
600
200
Y (m)
-200
0
200
400
600
X (m)
N013-N060
N136-N159
N028-N029
N051-N050
N151-N132
N109-N110
N151-N132
N109-N110
N136-N159
N051-N050
N028-N029
N013-N060
0
20
40
60
80
100
120
distance (m)

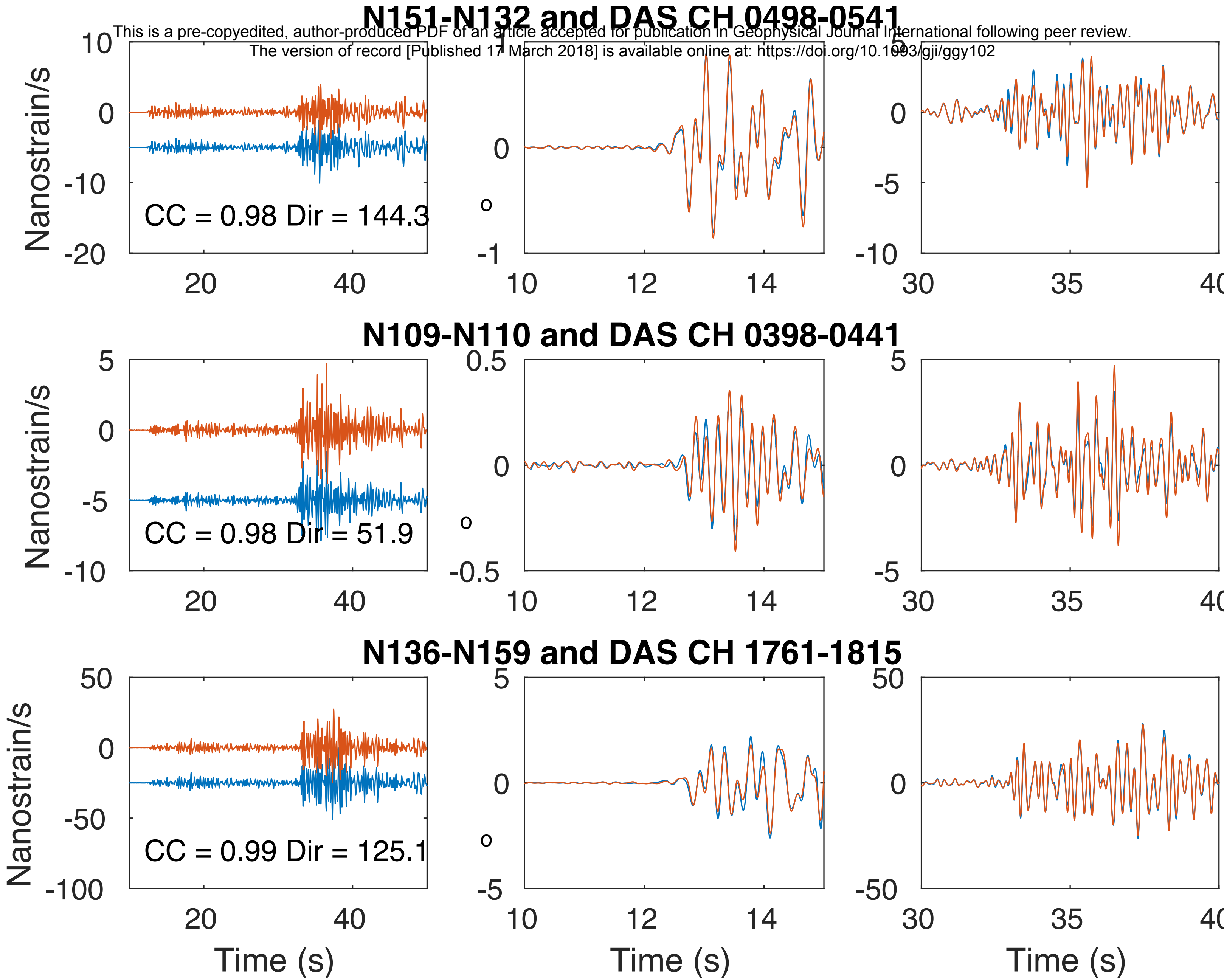
N151-N132 and DAS CH 0498-0541
Nanostrain/s
CC = 0.98 Dir = 144.3
o
N109-N110 and DAS CH 0398-0441
Nanostrain/s
CC = 0.98 Dir = 51.9
o
N136-N159 and DAS CH 1761-1815
Nanostrain/s
CC = 0.99 Dir = 125.1
o
Time (s)
Time (s)
Time (s)

Fig. 12

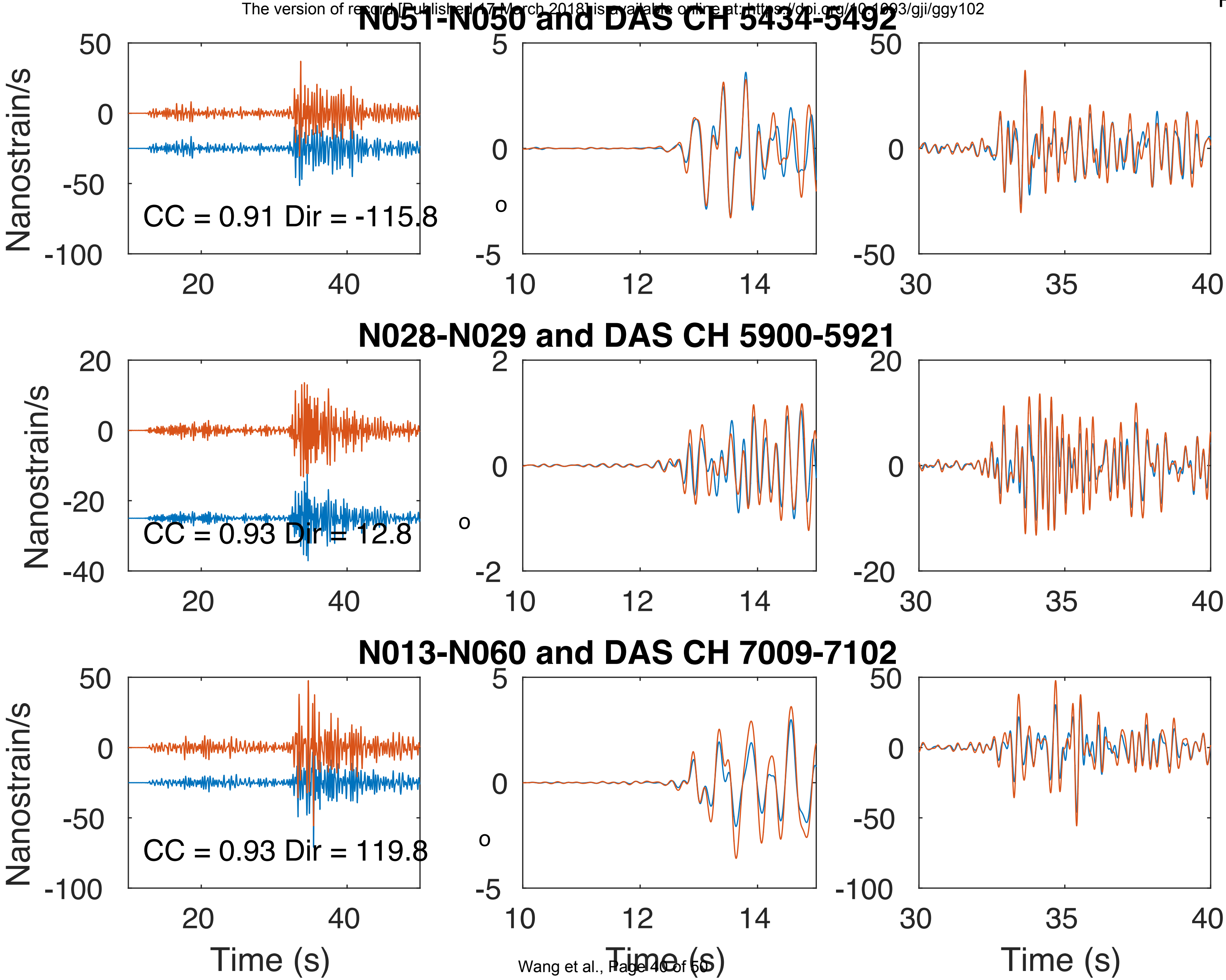
N051-N050 and DAS CH 5434-5492
Nanostrain/s
CC = 0.91 Dir = -115.8
o
N028-N029 and DAS CH 5900-5921
Nanostrain/s
CC = 0.93 Dir = 12.8
o
N013-N060 and DAS CH 7009-7102
Nanostrain/s
CC = 0.93 Dir = 119.8
o
Time (s)
Time (s)
Time (s)

Fig. 13

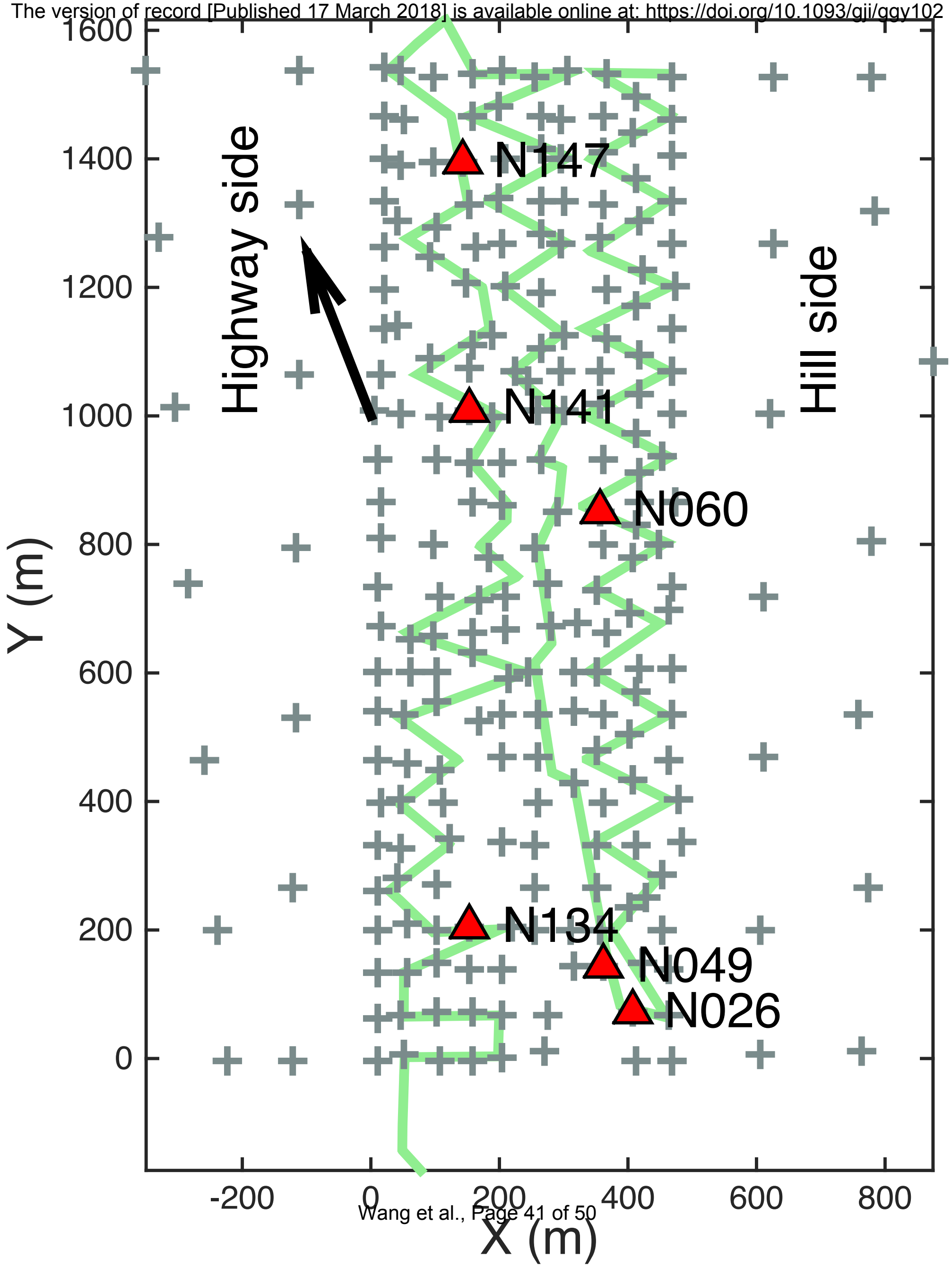
1600
1400
1200
1000
800
600
400
200
0
Y (m)
-200
0
200
400
600
800
X (m)
Highway side
Hill side
N147
N141
N060
N134
N049
N026

Fig. 14

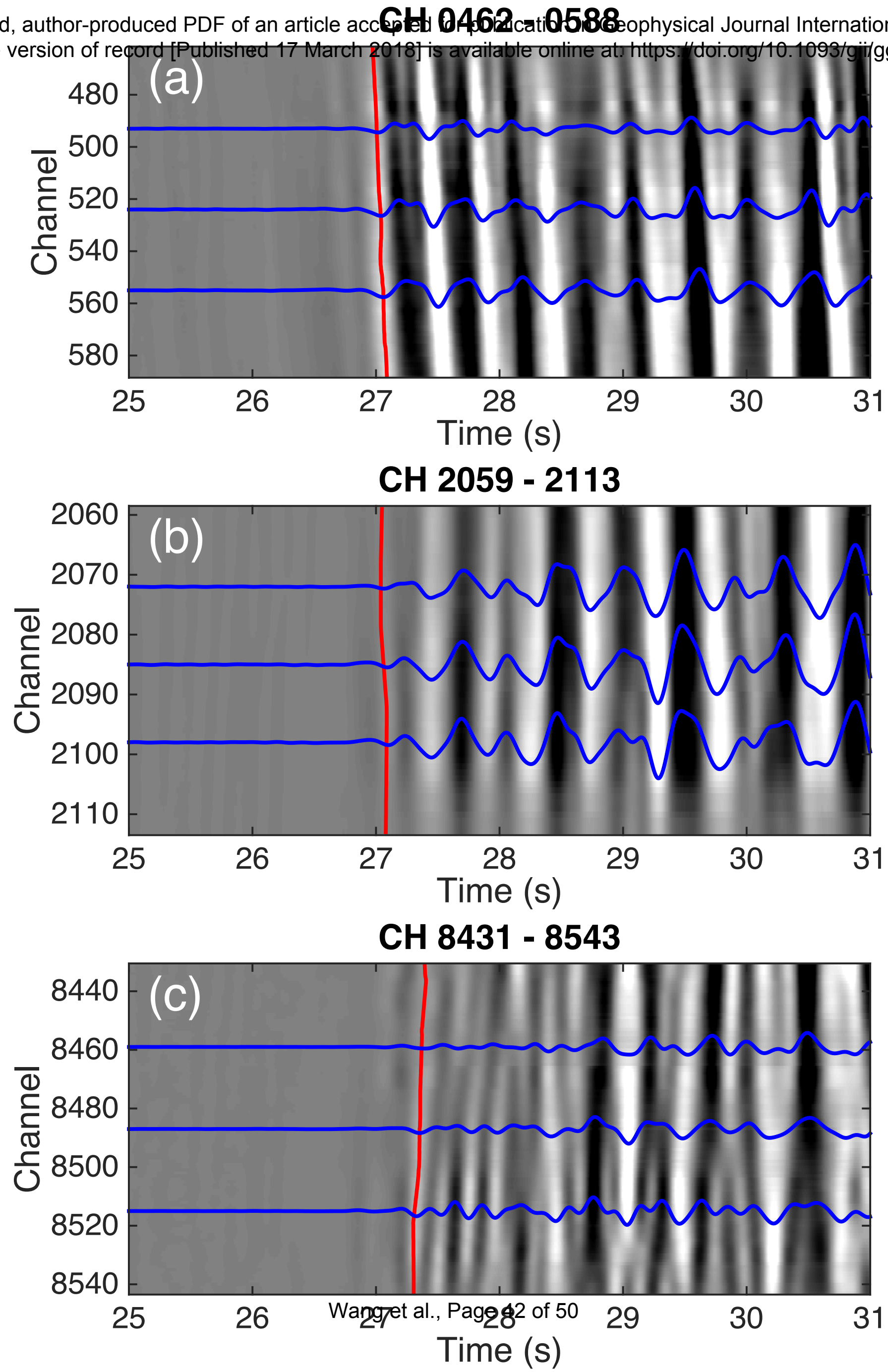
CH 0462 - 0588
(a)
Channel
480
500
520
540
560
580
25
26
27
28
29
30
31
Time (s)
CH 2059 - 2113
(b)
2060
2070
2080
2090
2100
2110
CH 8431 - 8543
(c)
8440
8460
8480
8500
8520
8540

Fig. 15

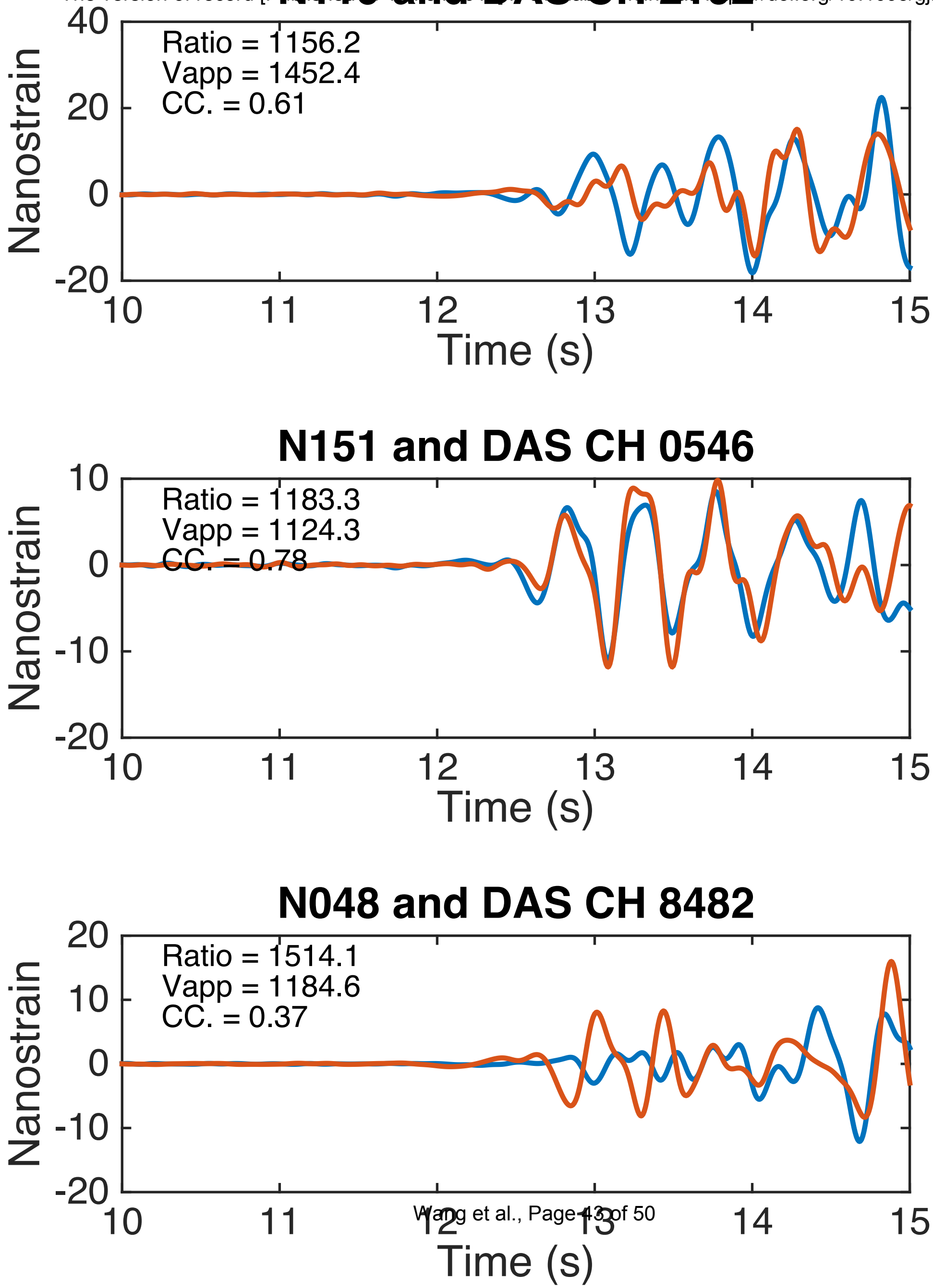
N119 and DAS CH 2102
Ratio = 1156.2
Vapp = 1452.4
CC. = 0.61
Nanostrain
Time (s)
N151 and DAS CH 0546
Ratio = 1183.3
Vapp = 1124.3
CC. = 0.78
Nanostrain
Time (s)
N048 and DAS CH 8482
Ratio = 1514.1
Vapp = 1184.6
CC. = 0.37
Nanostrain
Time (s)

Fig. 16

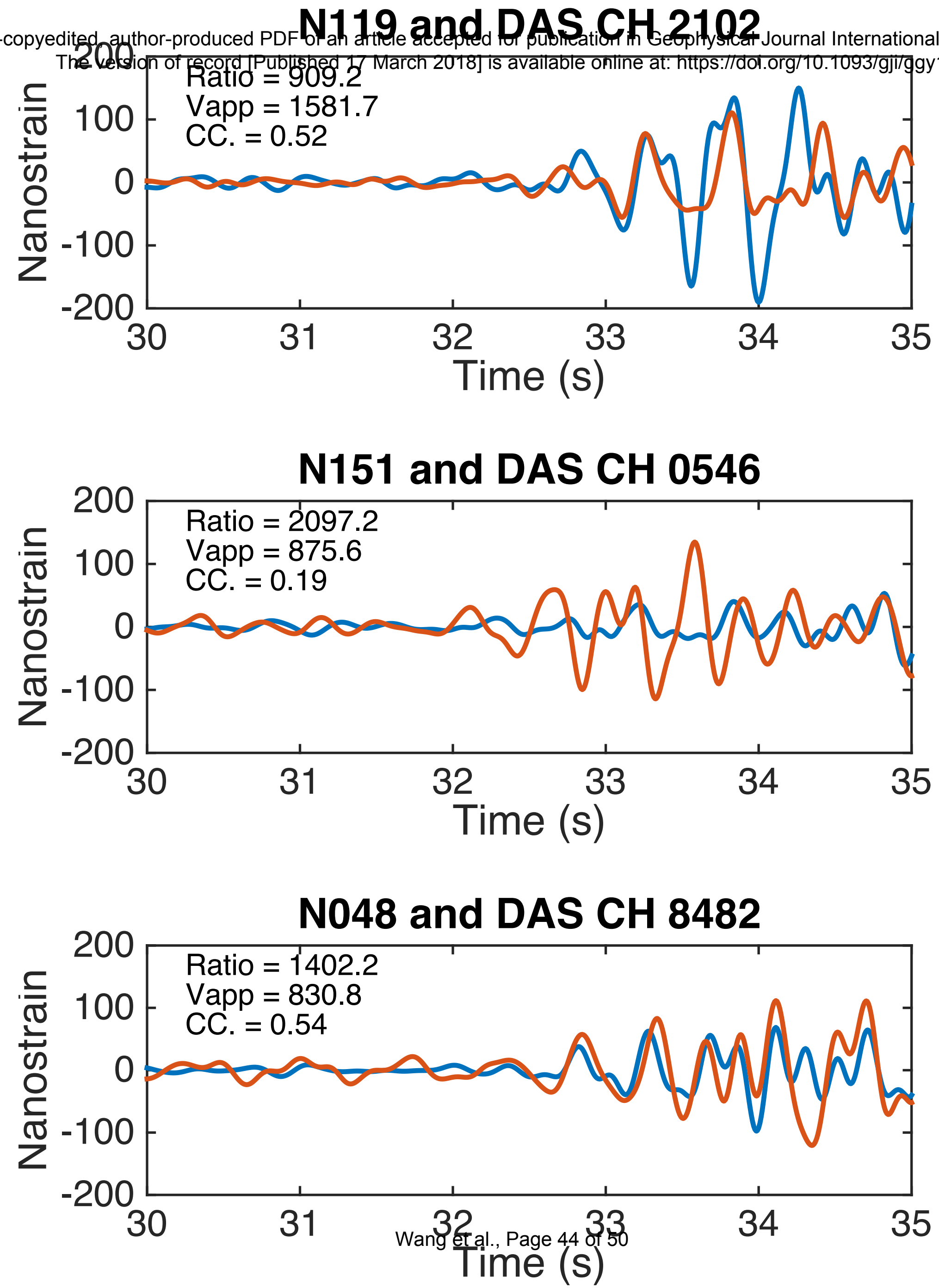
N119 and DAS CH 2102
Ratio = 909.2
Vapp = 1581.7
CC. = 0.52
Nanostrain
200
100
0
-100
-200
30
31
32
33
34
35
Time (s)
N151 and DAS CH 0546
Ratio = 2097.2
Vapp = 875.6
CC. = 0.19
Nanostrain
Time (s)
N048 and DAS CH 8482
Ratio = 1402.2
Vapp = 830.8
CC. = 0.54
Nanostrain
Time (s)

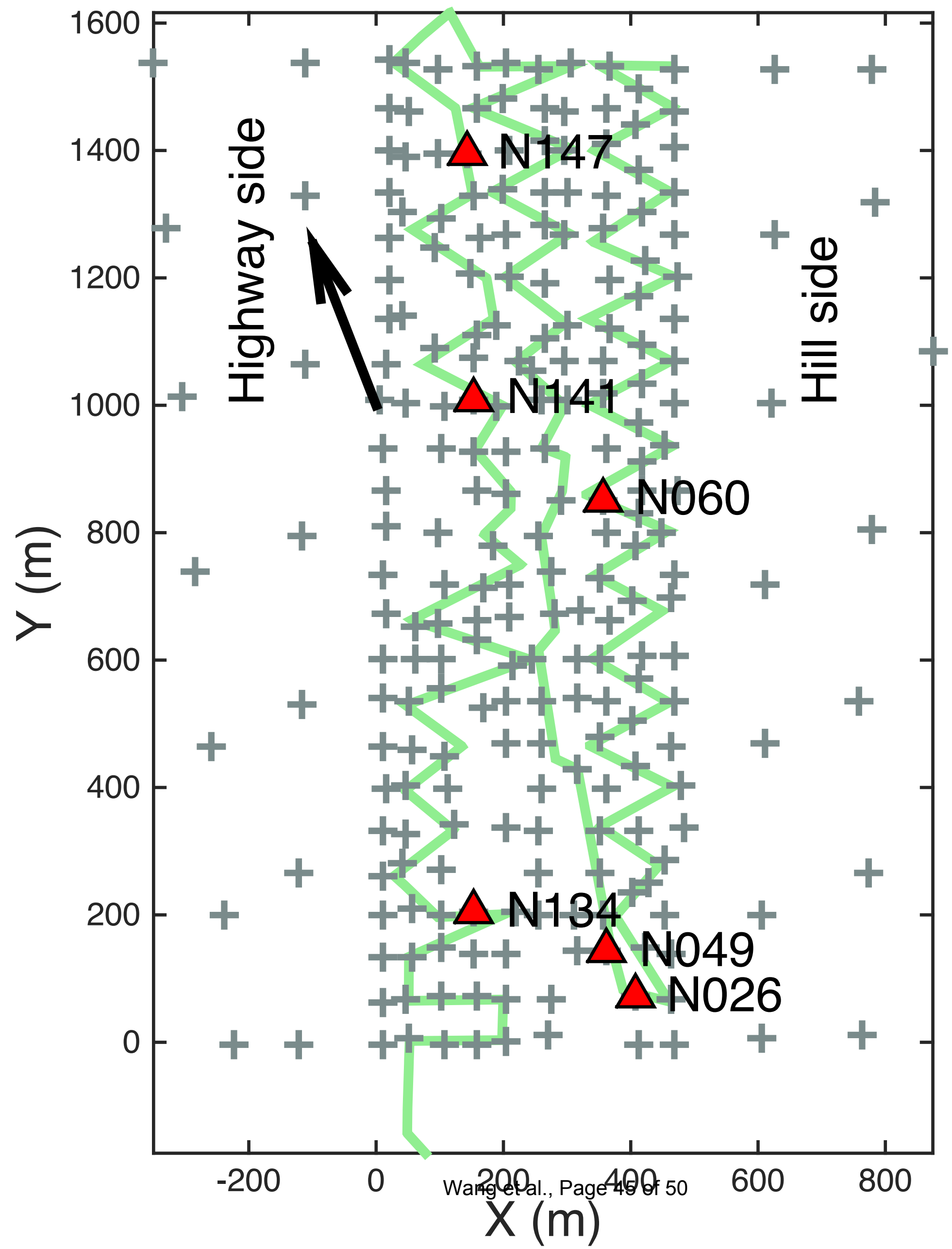
1600
1400
1200
1000
800
600
400
200
0
-200
0
200
400
600
800
Y (m)
X (m)
Highway side
Hill side
N147
N141
N060
N134
N049
N026

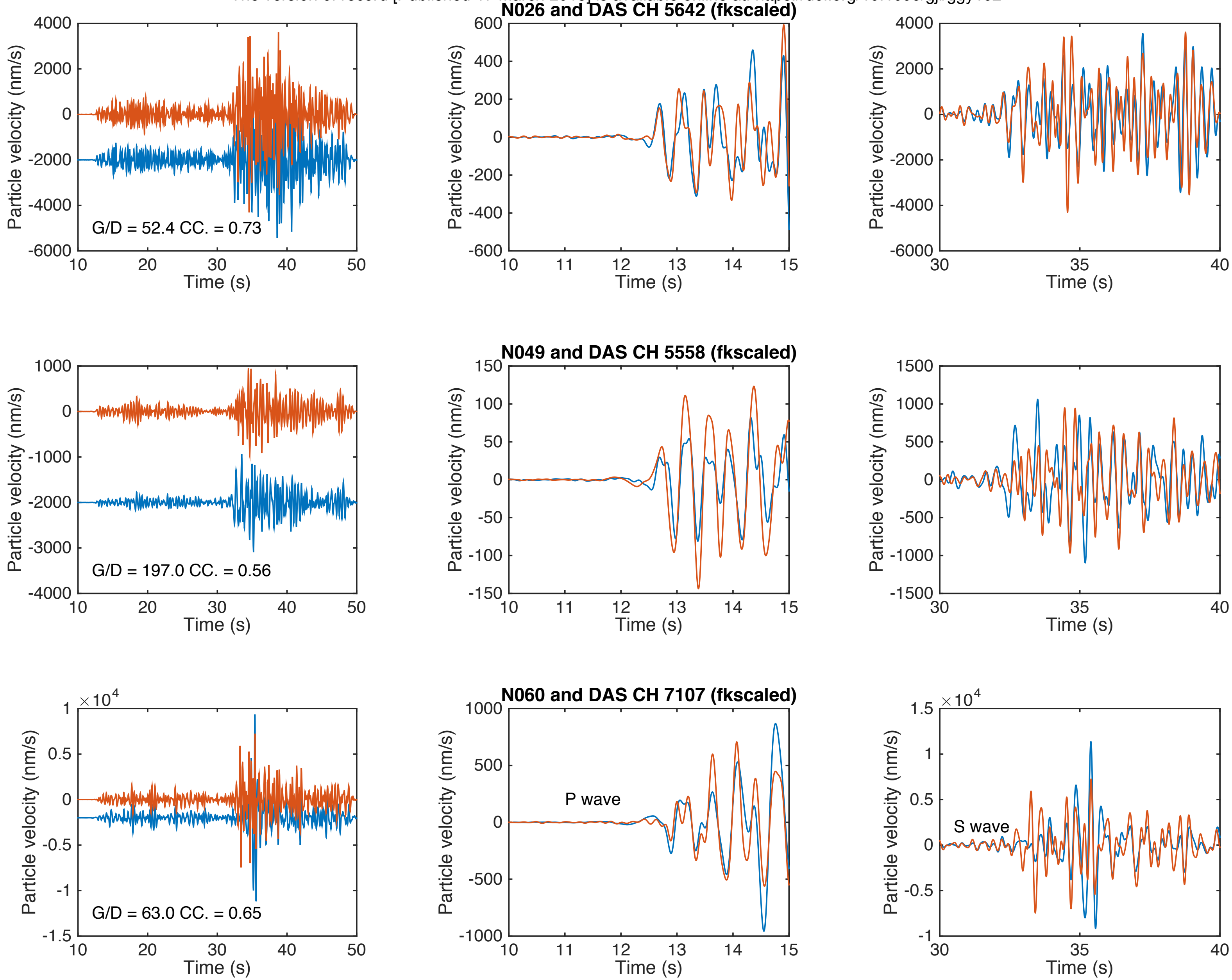
N026 and DAS CH 5642 (fkscaled)
N049 and DAS CH 5558 (fkscaled)
N060 and DAS CH 7107 (fkscaled)
Particle velocity (nm/s)
Time (s)
G/D = 52.4 CC. = 0.73
G/D = 197.0 CC. = 0.56
G/D = 63.0 CC. = 0.65
P wave
S wave
×10^4

Fig. 19

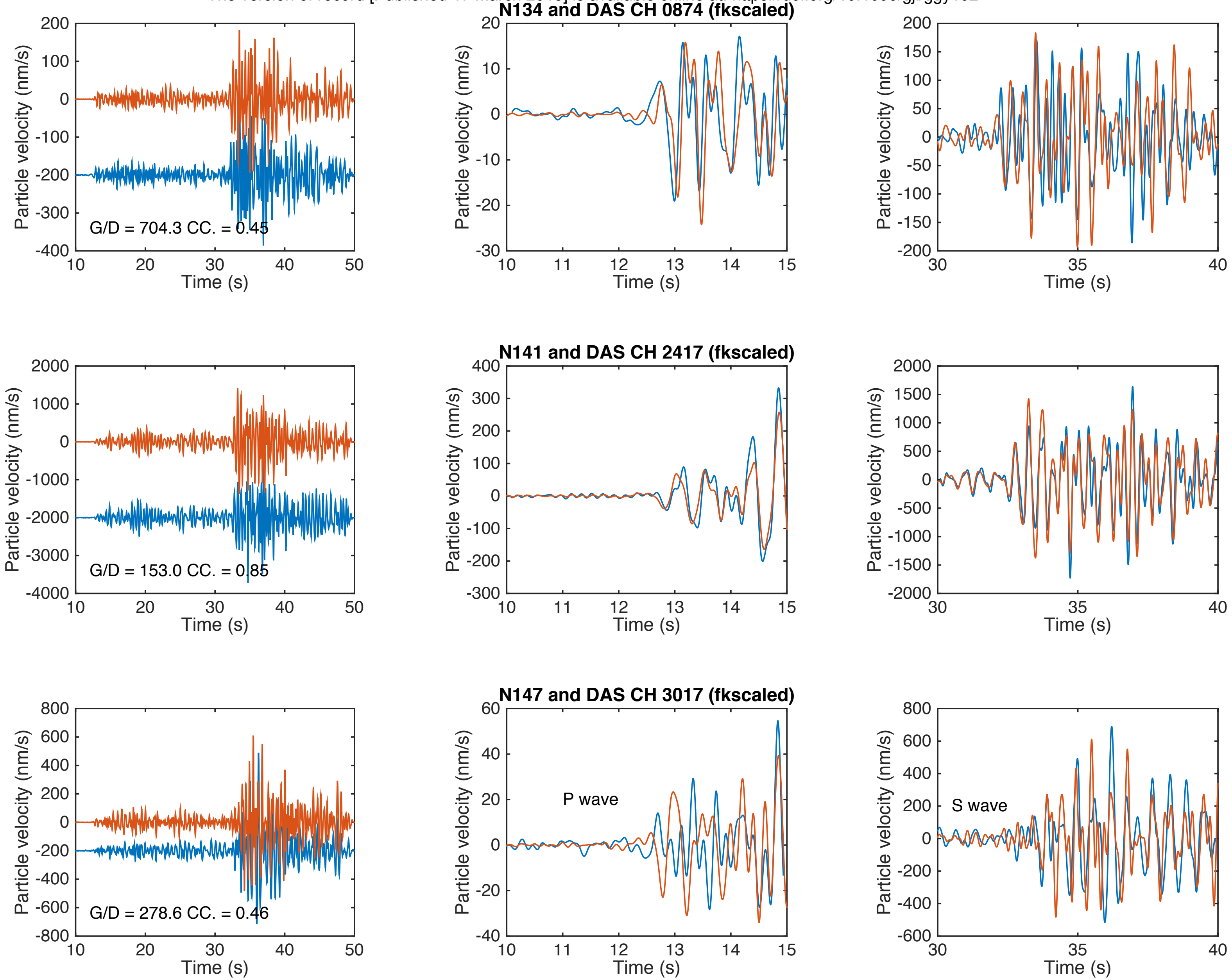
N134 and DAS CH 0874 (fkscaled)
N141 and DAS CH 2417 (fkscaled)
N147 and DAS CH 3017 (fkscaled)
G/D = 704.3 CC. = 0.45
G/D = 153.0 CC. = 0.85
G/D = 278.6 CC. = 0.46
P wave
S wave
Particle velocity (nm/s)
Time (s)

This is a pre-copyedited, author-produced PDF of an article accepted for publication in Geophysical Journal International following peer review.
The version of record [Published 17 March 2018] is available online at: https://doi.org/10.1093/gji/ggy102

Fig. 20

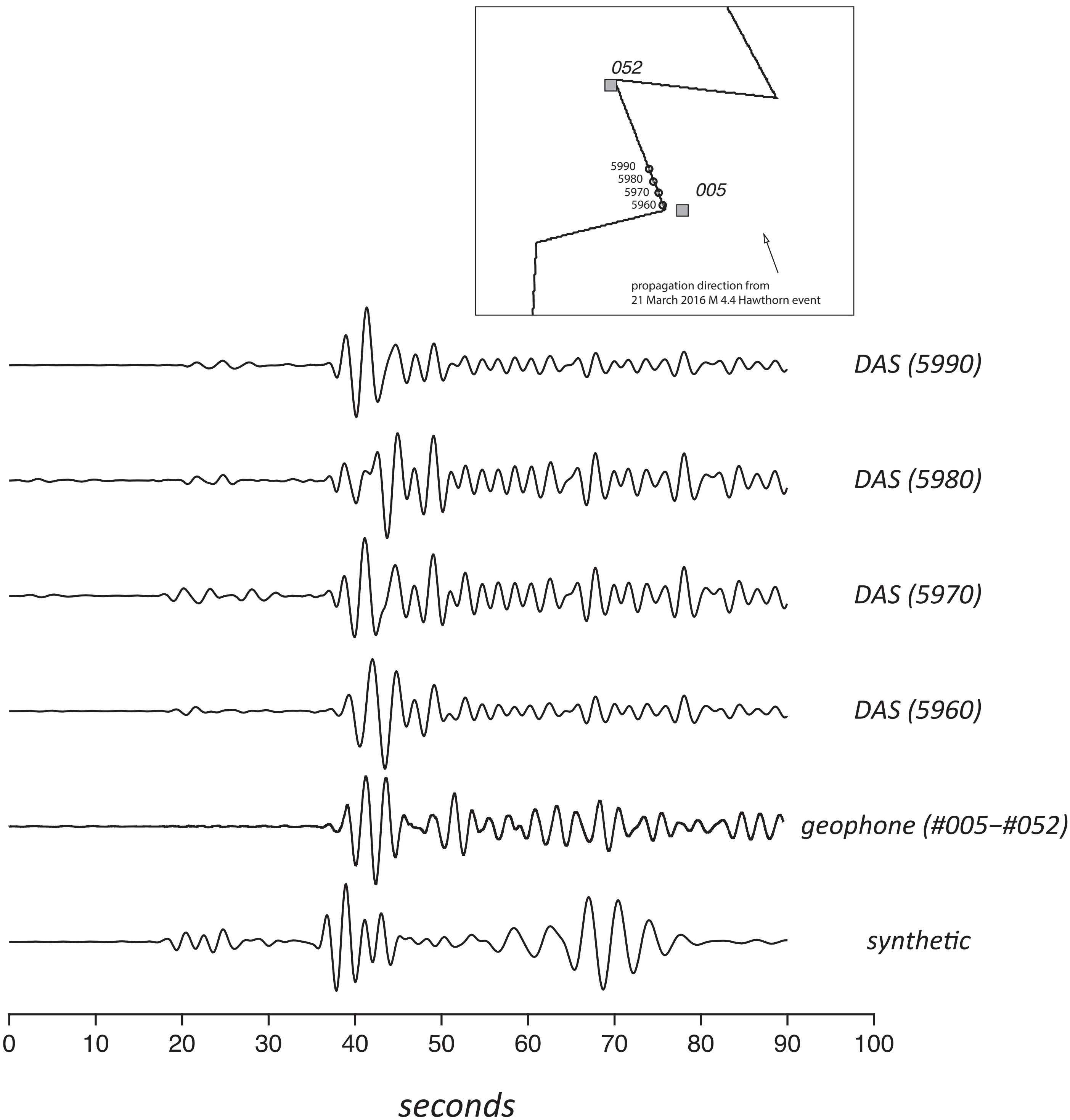

This is a pre-copyedited, author-produced PDF of an article accepted for publication in Geophysical Journal International following peer review.
The version of record [Published 17 March 2018] is available online at: https://doi.org/10.1093/gji/ggy102

Fig. 21

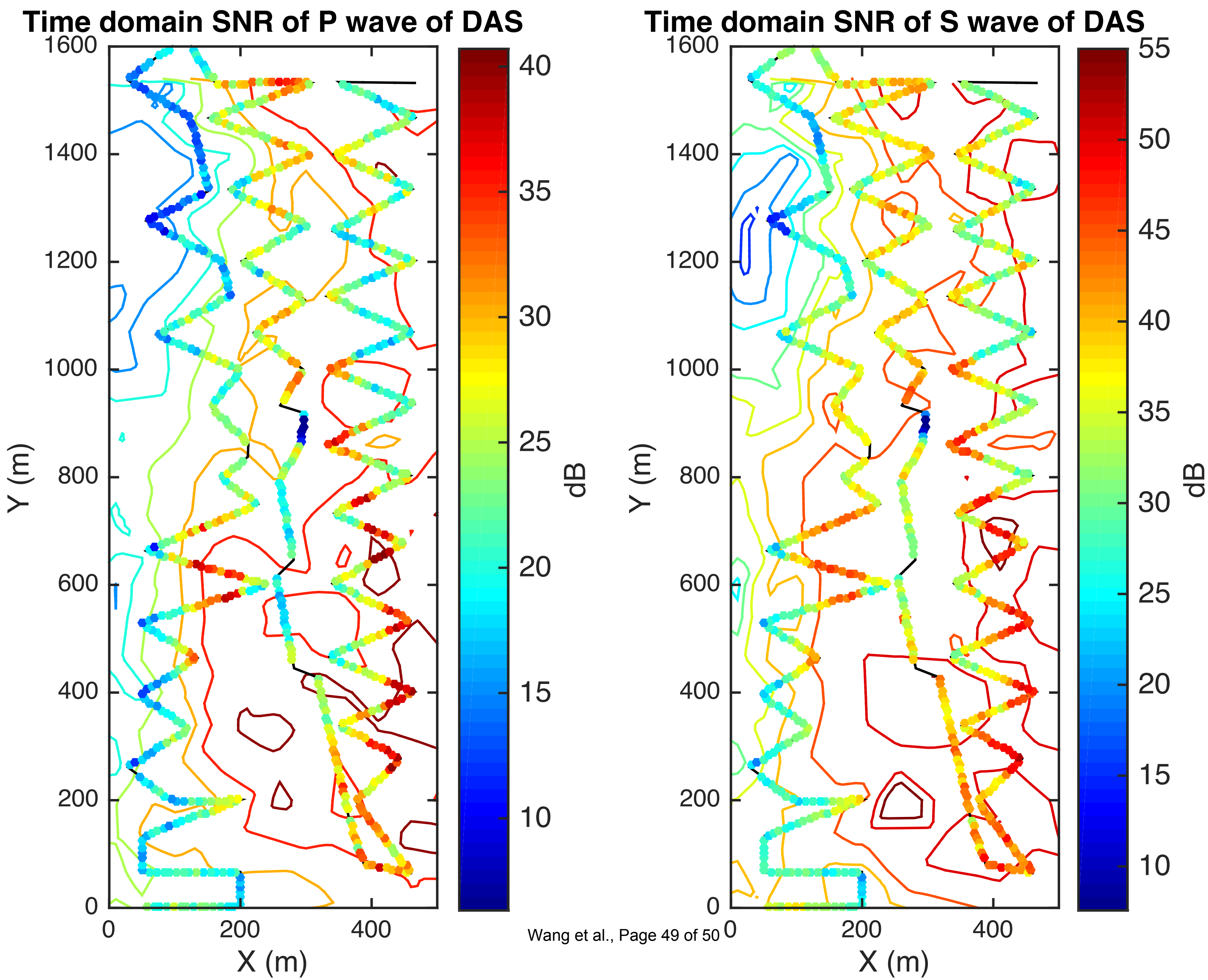

Fig. 22

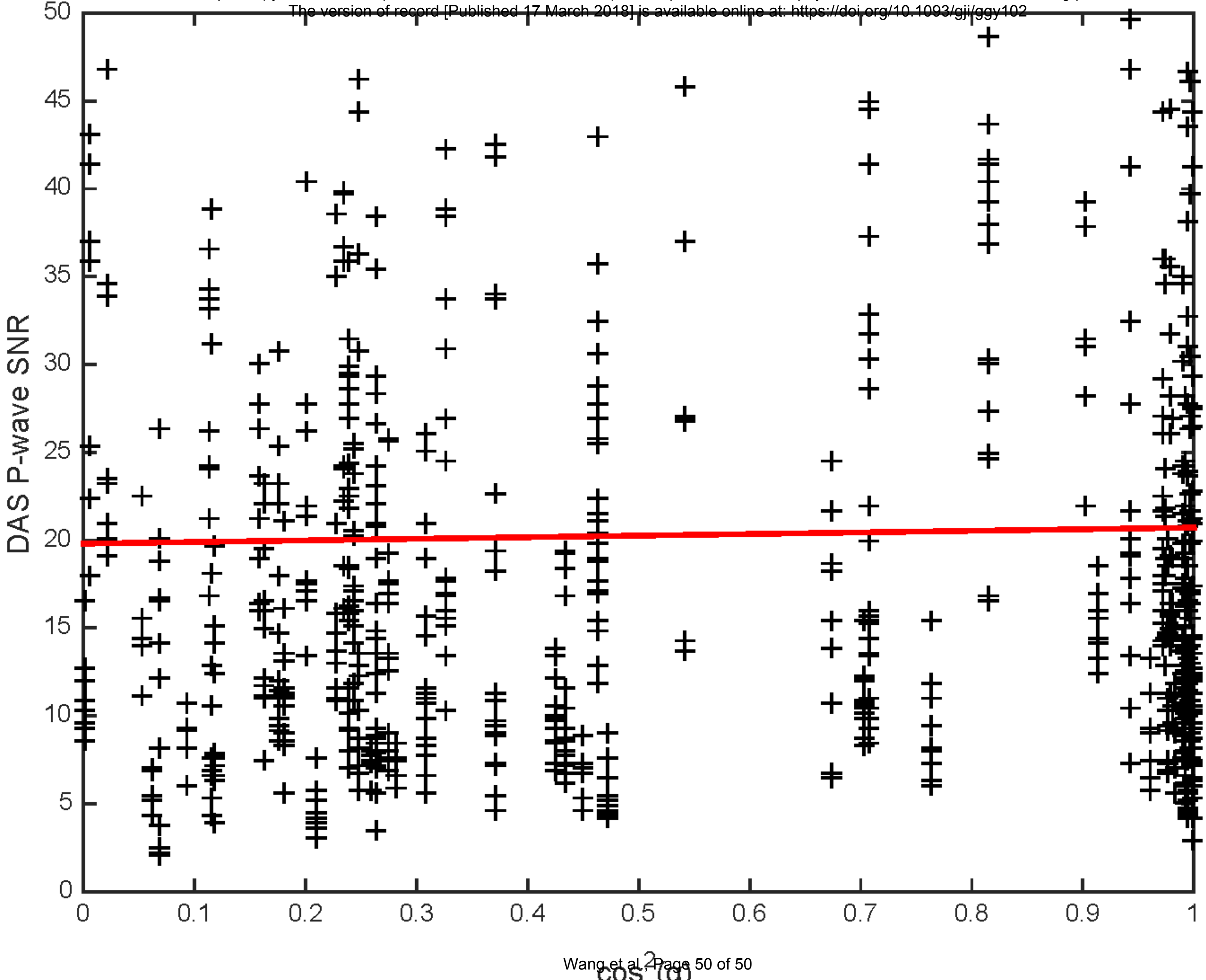
DAS P-wave SNR
$\cos^2(\alpha)$
0
5
10
15
20
25
30
35
40
45
50
0
0.1
0.2
0.3
0.4
0.5
0.6
0.7
0.8
0.9
1